Journal of Materials Chemistry A

REVIEW

View Article Online
View Journal | View Issue

Cite this: J. Mater. Chem. A, 2016, 4, 7107

Recent progress and perspectives on bi-functional oxygen electrocatalysts for advanced rechargeable metal–air batteries

Dong Un Lee,† Pan Xu,† Zachary P. Cano, Ali Ghorbani Kashkooli, Moon Gyu Park and Zhongwei Chen*

With continued dependence on carbon-based fuels and rising concerns of environmental issues, the development of rechargeable metal–air batteries has recently gained tremendous attention. However, due to the slow kinetics of electrochemical oxygen reactions, the charge and discharge processes of a rechargeable metal–air battery must be catalyzed by using bi-functional catalysts that are active towards both the oxygen reduction and oxygen evolution reactions. This review focuses on recent developments in bi-functional catalysts and their catalytic activity in relation to materials composition, morphology, and crystal structure obtained through various synthetic techniques. The discussion is divided into sections based on the main types of recent bi-functional catalysts such as transition metal- and carbon-based materials, and hybrids which consist of the two. The subsections are then divided based on the metal substituents, types of dopant, degree of doping, and defect densities, discussing the effects of composition. In parallel, morphological effects on the catalytic activity, such as unique nanostructured design, surface area enhancements, and porosity, are also discussed. Currently, bi-functional oxygen electrocatalyst research is heading in the direction of reducing the loading of precious metals, and developing cost-competitive non-precious metal- and carbon-based catalysts to enable commercialization of rechargeable metal–air batteries for various applications including electric-drive vehicles and smart-grid energy storage. To understand the origin of bi-functional catalytic activity, future catalyst research should be conducted in combination with *in situ* characterizations, and computational studies, which will allow exploitation of active sites to maximize the efficacy of bi-functional catalysts.

Received 7th January 2016
Accepted 31st March 2016

DOI: 10.1039/c6ta00173d

www.rsc.org/MaterialsA

1. Introduction

Price volatility and the negative impacts of emissions associated with using carbon-based fuel sources have presented a strong

Department of Chemical Engineering, Waterloo Institute for Nanotechnology, Waterloo Institute for Sustainable Energy, University of Waterloo, 200 University Ave. West, Waterloo, ON, Canada N2L 3G1. E-mail: zhwchen@uwaterloo.ca

† These authors contributed equally.

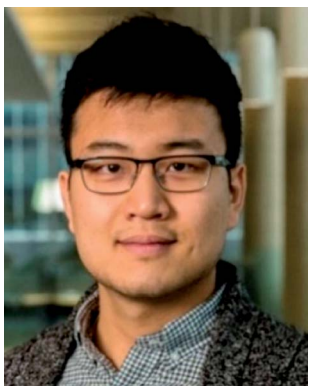

Dong Un Lee received his Bachelor's degree in Nanotechnology Engineering from the University of Waterloo in 2010. He is currently pursuing his Ph.D. degree in Chemical Engineering (Nanotechnology) under the supervision of Prof. Zhongwei Chen at the University of Waterloo. His research is mainly focused on the development of transition metal/carbon hybrid bi-functional electrocatalysts active towards oxygen reduction and oxygen evolution reactions for rechargeable metal–air batteries.

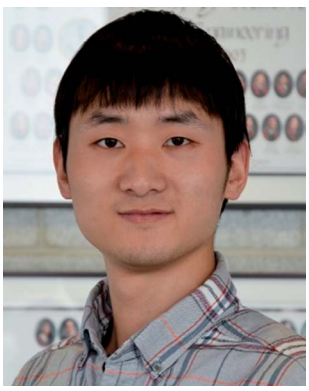

Pan Xu received his Master's degree under the supervision of Prof. Jinli Qiao from Donghua University (China) in 2015. He is currently pursuing his Ph.D. degree in Chemical Engineering under the supervision of Prof. Zhongwei Chen at the University of Waterloo. His current research focuses on the development of nanostructured oxygen electrocatalysts including bi-functional catalysts for fuel cells and rechargeable metal–air batteries.

driving force for the current generation to decrease its reliance on these forms of energy. However, global energy consumption is projected to increase by more than a third by 2040, with three quarters of this energy expected to occur within the next 10 years.[1] Thus, the accelerated development of reliable, inexpensive and environmentally friendly energy generation is of utmost importance for continued economic growth and geopolitical stability. In order to levelize the intermittent output of low-carbon sources such as solar and wind energy, various types of energy conversion and storage systems have been developed such as fuel cells, batteries and supercapacitors. In particular, the demand for inexpensive and electrically rechargeable systems has led to tremendous interest in the development of rechargeable metal–air batteries for various applications such as smart-grid energy storage and electric vehicle propulsion.

Rechargeable metal–air batteries operate based on two fundamental electrochemical reactions, oxygen reduction reaction (ORR) and oxygen evolution reaction (OER), corresponding to the discharge and charge processes, respectively, offering a very high energy density and stable discharge voltage.[2,3] Unlike primary (non-rechargeable) metal–air batteries, electrically charging a secondary metal–air battery presents many technical challenges, the main one being the necessity to catalyze both ORR and OER using a bi-functionally active electrocatalyst. Until now, much of the catalyst research has been focused on either the oxygen reduction (applicable to fuel cells) or oxygen evolution (applicable to water splitting) reactions, but not both on the same catalyst surface. One of each of these electrocatalysts can be composited to fabricate a rechargeable air electrode, but this requires the synthesis of two different materials, which raises cost concerns and introduces manufacturing complexities. Alternatively, recent advancements in catalyst development have made possible the fabrication of rechargeable air electrodes using a single active material that is capable of bi-functionally catalyzing both oxygen reactions (Fig. 1). This has fueled the development of highly active and durable bi-functional catalysts in the past few decades specifically for rechargeable metal–air batteries, such as lithium–air and zinc–air batteries. In fact, rechargeable

Zachary P. Cano received his Bachelor's degree (2012) and Master's degree (2015) in Materials Science and Engineering from McMaster University, where he specialized in corrosion science. He is now pursuing his Ph.D. in Chemical Engineering (Nanotechnology) under the supervision of Prof. Michael Fowler and Prof. Zhongwei Chen at the University of Waterloo. His research is currently focused on the development of novel anode structures and cell designs for long-lasting rechargeable metal–air batteries.

Ali Ghorbani Kashkooli is currently a Ph.D. candidate in Chemical Engineering at the University of Waterloo under the supervision of Prof. Zhongwei Chen. His research interest mainly focuses on modeling and development of electrochemical energy storage and convergence systems including lithium-ion batteries, zinc–air batteries, and supercapacitors.

Moon Gyu Park received his Master's degree in Chemical Engineering from the University of Waterloo in 2015. He is currently pursuing his Ph.D. degree in Chemical Engineering at the University of Waterloo under the supervision of Prof. Zhongwei Chen. His current research interests lie in the development of non-precious transition metal-based materials and nanostructured metal/carbon composites as bi-functional electrocatalysts for rechargeable metal–air battery applications.

Dr Zhongwei Chen is Canada Research Chair Professor in Advanced Materials for Clean Energy at the University of Waterloo. His research interests are in the development of advanced energy materials for metal–air batteries, lithium-ion batteries and fuel cells. He was promoted to an Associate Professor with early tenure in 2012, was awarded the Canada Research Chair in 2014 and Steacie Memorial Fellowship in 2016. He has published 1 book, 6 book chapters and more than 150 peer-reviewed journal articles with over 10 000 citations and H-index of 44 (Google Scholar). He is listed as an inventor on 15 US/international patents, with several licensed to companies in USA and Canada.

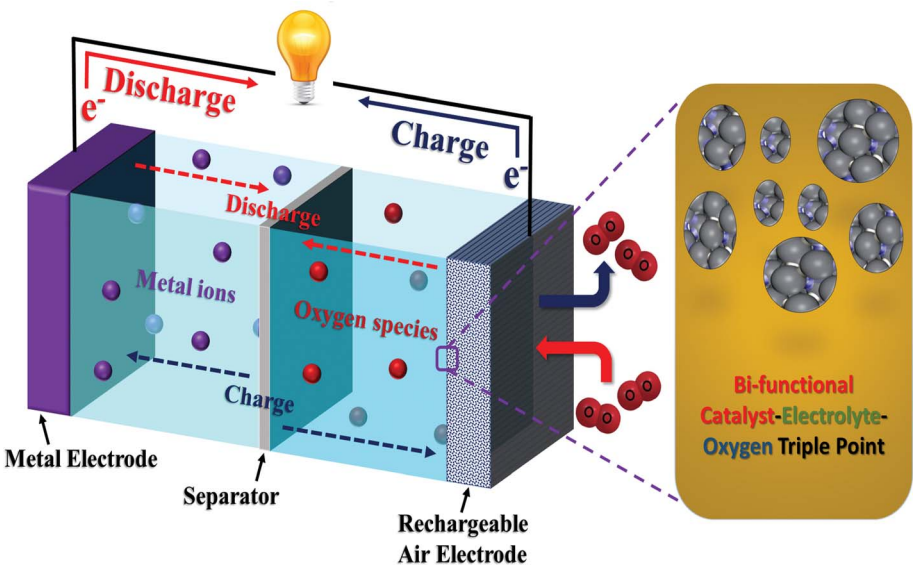

Fig. 1 Schematic illustration of a rechargeable metal–air battery and its operating principle based on the electrochemical oxygen reactions occurring on a bi-functionally active catalyst.

metal–air batteries are considered potentially the most viable energy system to replace the matured lithium-ion battery technology that is expensive and has almost reached its theoretical performance limits.

Currently, a large portion of studies on bi-functional oxygen catalysts is done in alkaline electrolytes, such as potassium hydroxide (KOH) and sodium hydroxide (NaOH), since these electrolytes allow replacement of expensive precious metal catalysts (such as platinum and iridium on carbon) with non-precious metal and/or metal-free catalysts due to their less corrosive nature compared to acidic electrolytes. Additionally, alkaline electrolytes are known to favor electrocatalytic oxygen reactions, allowing a significantly faster rate than acidic electrolytes.[4] Among many, the rechargeable zinc–air battery has been considered one of the most promising aqueous metal–air battery technologies due to its low cost, high energy density, environmental benignity, and safe operation. The research and development of zinc–air batteries dates back to the 1970s where the use of abundant and non-toxic metallic zinc anodes combined with the ORR at the air cathode were shown to provide high energy density and moderate cycle life.[5] In fact, the primary zinc–air battery is the only type of commercial metal–air battery, finding its application in niche markets such as hearing aids and transportation signals. With recent advancements in bi-functional catalyst development, zinc–air battery research has reemerged with emphasis on electrical rechargeability. Rechargeable zinc–air batteries have notable advantages over lithium-ion batteries that are currently widely employed, such as higher energy density, environmental benignity and lower cost.[3,6] In terms of safety, due to the non-toxic and non-volatile nature of zinc, zinc–air batteries can be produced and operated in open environments since metallic zinc does not react violently in the presence of moisture in air. The air electrode of zinc–air batteries is very similar to that of a fuel-cell, hence the knowledge of fuel cell technologies and systems already developed for commercial fuel cell technologies can be exploited for the development of commercial rechargeable zinc–air batteries.[6] The performances of various rechargeable and metal–air batteries in terms of gravimetric and volumetric energy densities are summarized in Fig. 2.

Based on reports found in the literature, bi-functional catalysts can be classified into three broad groups: non-precious metal catalysts, carbon-based materials, and hybrids which consist of the former two. Non-precious catalysts are further classified into oxides, sulfides, nitrides, *etc.*, and the oxides are found in different crystal structures such as spinels, perovskites, and pyrochlores. Carbon-based materials have recently gained attention due to the popularity of graphitic carbons such as carbon nanotubes and graphene nanosheets. However, carbon based catalyst research is still in its infancy, and the electrochemical instability of carbon poses technical challenges for bi-functional applications.[7,8] Hybrid catalysts which consist of both metal oxide and carbon address the inherently low

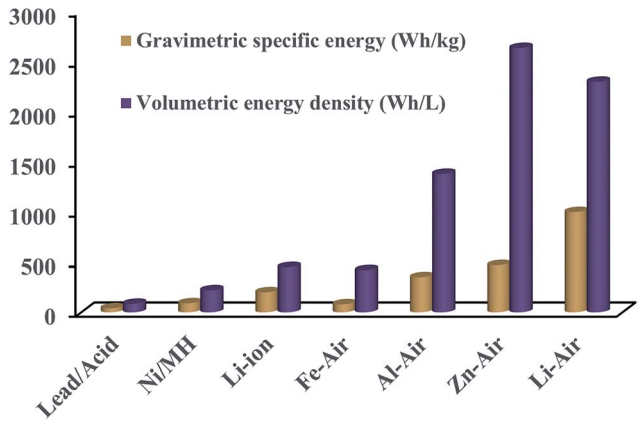

Fig. 2 Practical gravimetric specific energy and volumetric energy density of various types of rechargeable and metal–air batteries.

electrical conductivity of transition metal oxides while improving the stability of carbon. Graphitic carbon based materials in particular have been found to be very effective as supporting structures for non-precious metal catalysts, synergistically enhancing the catalytic performance. This review covers all of the articles published in the literature which are specifically focused on catalysts that are bi-functionally active. This is different from other recently published review papers on oxygen catalysis which focus on either ORR or OER and lack appropriate connections between the two for readers who seek literature on bi-functionally active catalysts. Additionally, even though a much greater portion of bi-functional catalyst research is conducted in alkaline aqueous electrolytes, which are pertinent to rechargeable zinc–air batteries, there seems to be a consistent positive correlation between the catalytic activity of aqueous and non-aqueous electrolytes. This means that bi-functional catalysts introduced in this review can be readily applied to non-aqueous rechargeable metal–air systems such as lithium–air and sodium–air batteries. Non-aqueous lithium–air batteries have recently gained tremendous attention due to their extremely high energy density comparable to that of gasoline powered engines. Hence, the discussion in this review is not limited to bi-functional oxygen catalysis in aqueous electrolytes, but rather promotes advancements in various types of rechargeable metal–air systems including ones that utilize non-aqueous electrolytes.

2. Oxygen electrocatalytic reactions

As mentioned above, the two primary electrochemical reactions catalyzed by bi-functionally active catalysts are oxygen reduction and oxygen evolution reactions, which correspond to discharge and charge processes of a metal–air battery, respectively. The roles of bi-functional catalysts are critically important for practical operation of metal–air batteries due to the intrinsically sluggish kinetics of the un-catalyzed ORR and OER. Briefly, the ORR proceeds by diffusion followed by adsorption of oxygen molecules onto a catalyst surface. Electrons drawn from the anode are subsequently transferred to the adsorbed oxygen, weakening and breaking the oxygen double bond. Finally, hydroxide ions are removed from the catalyst surface to the alkaline electrolyte.[9] Unlike ORR, the OER is much more difficult to describe because of a series of complex electrochemical reactions with multi-step electron-transfer processes.[10–12] However, to facilitate a better understanding of this review, the mechanisms of ORR and OER are described to an appropriate extent in the following sections.

2.1 Oxygen reduction reaction (ORR)

The two types of classical oxygen catalysts are metals and metal oxides, and the mechanism of the ORR using these catalysts has been intensively studied. For metal-based catalysts such as platinum, a four-electron pathway or a two-electron pathway may proceed for the ORR, depending on the type of oxygen adsorption.[10,13] There are two adsorption types: bidentate O_2 adsorption (two O atoms coordinate with the metal) and end-on O_2 adsorption (one O atom coordinates perpendicularly to the metal), which lead to the direct four-electron pathway and two-electron pathway, respectively.[14]

The reactions of the bidentate adsorption are as follows:

$$O_2 + 2H_2O + 2e^- \rightarrow 2OH_{ads} + 2OH^-$$

$$2OH_{ads} + 2e^- \rightarrow 2OH^-$$

$$\text{Overall: } O_2 + 2H_2O + 4e^- \rightarrow 4OH^-$$

For the end-on adsorption, the reactions are as follows:

$$O_2 + H_2O + e^- \rightarrow HO_{2,ads} + OH^-$$

$$HO_{2,ads} + e^- \rightarrow HO_2^-$$

$$\text{Overall: } O_2 + H_2O + 2e^- \rightarrow HO_2^- + OH^-$$

The above two-electron reaction may be followed by either a further two-electron reduction of peroxide or by chemical disproportionation of peroxide as follows:

$$HO_2^- + H_2O + 2e^- \rightarrow 3OH^- \text{ (peroxide reduction)}$$

Or

$$2HO_2^- \rightarrow 2OH^- + O_2 \text{ (peroxide disproportionation)}$$

For metal oxide catalysts, such as spinel Co_3O_4, the ORR reaction pathways at the surface follow the same principle, but with a different charge distribution, due to the surface cations of stoichiometric oxides that are not fully coordinated with oxygen atoms. In aqueous electrolytes, anion coordination is completed by the oxygen of a water molecule. Consequently, the reduction of a surface cation by an electron from the external circuit is charge-compensated by protonation of a surface oxygen ligand.[15] The reaction pathway of ORR on a metal oxide surface is as follows:

$$2M^{m+}\text{–}O^{2-} + 2H_2O + 2e^- \rightarrow 2M^{(m-1)+}\text{–}OH^- + 2OH^-$$

$$O_2 + e^- \rightarrow O_{2,ads}^-$$

$$2M^{(m-1)+}\text{–}OH^- + O_{2,ads}^- + e^- \rightarrow 2M^{m+}\text{–}O^{2-} + 2OH^-$$

The ORR pathways and mechanisms may vary depending on the catalyst used and its electronic structure. For instance, the degree of the σ* orbital and the metal–oxygen covalency has influence on the competition between O_2^{2-}/OH^- displacement and OH^- regeneration on the surface of transition metal ions as the rate-determining steps of the ORR. Hence, correctly tuning the electronic structure of metal oxide catalysts by optimization of the composition is crucial for obtaining high performance catalysts.[16] It is also important to note that the oxygen reduction

occurs at the catalyst-electrolyte-oxygen triple point, which highlights the importance of maximizing the number of sites shared by all three solid-liquid-gas phases.

2.2 Oxygen evolution reaction (OER)

The OER pathways and mechanisms are relatively complex. Generally, oxygen is evolved from an oxide phase, rather than a bare metal,[12,15] which means that the mechanisms may vary depending on the catalyst having different site geometries of metal cations. The multi-valence characteristics of transition metal ions are important for OER because the reaction is induced by the interaction between the metal ions and oxygen intermediates which leads to the formation of a bond by changing the valence state. The site geometry of metal cations changes the adsorption energy of the oxygen species, which determines the kinetics of OER. For a transition metal oxide catalyst containing surface reactions M^{m+}–O^{2-} = $M^{(m-1)+}$–O^{-} biased towards the right-hand side, the OER in alkaline electrolyte proceeds as follows:

$$M^{m+}\text{–}O^{2-} + OH^{-} \rightarrow M^{(m-1)+}\text{–}O\text{–}OH^{-} + e^{-}$$

$$M^{(m-1)+}\text{–}O\text{–}OH^{-} + OH^{-} \rightarrow M^{m+}\text{–}O\text{–}O^{2-} + H_2O + e^{-}$$

$$2M^{m+}\text{–}O\text{–}O^{2-} \rightarrow 2M^{m+}\text{–}O^{2-} + O_2$$

Typically, precious metal oxides such as RuO_2 and IrO_2 are known to be highly active towards OER due to low redox potential and high electrical conductivity. However, these precious metal-based oxides are very costly and have only demonstrated limited ORR activity, insufficient for use as bi-functional catalysts for rechargeable metal–air batteries. Conversely, much more cost effective and strongly bi-functional transition metal oxide catalysts such as Co_3O_4 and $NiCo_2O_4$ have shown high activities for both OER and ORR with electrochemical stability.

3. Non-precious metal-based materials

One of the main purposes of research on bi-functional oxygen catalysts is to focus on using them as rechargeable air electrodes for secondary metal–air batteries. Rechargeable zinc–air batteries in particular utilize aqueous alkaline electrolytes, which allows the use of non-precious metal-based catalysts due to the electrolyte's relatively low corrosivity. Hence, a large number of recently published reports belong to this group, and they demonstrate sufficiently high bi-functional oxygen reaction rates with some performing comparably to precious metal benchmark catalysts. Most of the reported catalysts are metal oxides, but other compounds such as nitrides and sulfides are also reported to exhibit bi-functional activity. These catalysts are divided into different sections based on their crystal structure and their bi-functional catalytic activities are discussed in detail.

3.1 Single metal oxides

Bi-functional electrocatalysts made of single metal oxides are simple in composition yet effective in facilitating oxygen reactions.[17–35] Manganese oxides (MnO_2, Mn_2O_3, Mn_3O_4, *etc.*) are one of the most investigated and utilized single metal oxide oxygen catalysts due to their affordability and environmental benignity. As such they are found commonly in commercial alkaline batteries and primary zinc–air batteries. For OER, manganese oxide catalysts have been synthesized and studied extensively by various groups,[36–38] leading to both theoretical and experimental results showing that higher oxidation states of Mn ions are more favorable for OER.[30,37] On the other hand, for ORR, Mao *et al.* found that manganese oxide catalysts promote the two-electron chemical disproportionation of HO_2^-, which allows the overall reaction to occur in the four-electron ORR pathway from O_2 to OH^-.[39] However, as opposed to two separate two-electron transfer processes, some researchers have reported that the Mn^{III}/Mn^{IV} redox couple acts as an oxygen acceptor–donor promoting the ORR to occur in the direct four-electron reduction pathway.[40,41] In this case, the quasi-equilibrium proton insertion process in MnO_2 leads to the formation of MnOOH, two of which subsequently bind with an O_2 molecule to reduce it to OH^-. In general, the degree of utilization of specific oxidation states of a transition metal ion is closely associated with the exposed crystallographic orientations which are in turn controlled by the morphology of catalysts. These various factors that affect the overall activity of manganese oxide bi-functional catalysts will be further explored in this section.

Inspired by nature's cubane-like $CaMn_4O_x$ catalyst which is known to facilitate water oxidation, Gorlin *et al.* developed a thin-film analogue composed of Mn^{III} oxide (α-Mn_2O_3), which exhibited excellent bi-functional oxygen electrocatalytic activities similar to the activities of Pt, Ru, and Ir precious metal-based catalysts.[19] In their later work, *in situ* X-ray absorption spectroscopy (XAS) analysis was conducted to reveal that the phase of MnO_x changed between ORR and OER, resulting in the disordered $Mn_3^{II,III,III}O_4$ phase and a mixture of two coexisting MnO_x phases, $Mn^{III,IV}$ oxide and less oxidized $Mn_3^{II,III,III}O_4$, after ORR and OER sweep, respectively.[20] The $Mn^{III,IV}$ oxide phase is found to be more dominant on the catalyst surface after OER due to electrochemical oxidation at the OER potential, indicating that it is the phase pertinent to OER. Such phase changes were also confirmed by theoretical predictions and experimental results in their former work.[30] These reversible phase changes observed with metal oxide catalysts emphasize the fact that the oxidation state of the catalyst surface is important in facilitating high bi-functional activity. The importance of surface crystallinity on the electrocatalytic activity was highlighted in the work by Kuo *et al.*, where novel nanostructures of MnO such as octahedral nanoparticles, nano-flowers and nano-polypods were synthesized by thermal decomposition of $Mn(oleate)_2$, resulting in the exposure of different crystal facets.[23] The electrochemical investigation of these catalysts showed that preferentially exposed (100) planes of MnO nano-polypods showed ORR and OER activities both superior than those of MnO nano-flowers.

Meng *et al.* also investigated the influence of different crystallographic structures of MnO_2 such as α-MnO_2, β-MnO_2, δ-MnO_2, and amorphous MnO_2 (AMO) on bi-functional oxygen catalytic activity (Fig. 3a).[25] Additionally, various morphologies of MnO_2 such as nanowires, nanoflakes, and nanoparticles were obtained during the synthesis of different crystal structures of MnO_2 (Fig. 3b–g). Based on half-cell electrochemical activity evaluation, the degrees of both ORR and OER activities were found to follow the order of α-MnO_2 > AMO > β-MnO_2 > δ-MnO_2 (Fig. 3h and i, respectively). Similarly, Débart and co-workers found that α-MnO_2 gave the highest charge storage capacity as compared to β-MnO_2, γ-MnO_2, λ-MnO_2, Mn_2O_3, and Mn_3O_4, exceeding 3000 mA g^{-1} based on the evaluation using a rechargeable lithium–air battery.[18] This is a prime example of a bi-functional catalyst used in aqueous electrolytes demonstrating excellent performance in an aprotic non-aqueous lithium–air battery. However, the catalytic pathway is different in non-aqueous electrolytes since the crystal structure of α-MnO_2 consisting of 2 × 2 tunnels formed by edge- and corner-sharing MnO_6 octahedra is known to well accommodate Li_2O within the tunnels, with the O_2 ions located at the tunnel centers and the Li^+ ions coordinated between these central O_2 ions. In the same work, various nanoscale morphologies of MnO_2 were studied and it was found that MnO_2 nanowires surpassed bulk MnO_2 in catalytic activity. Interestingly, both α- and β-phases of MnO_2 nanowire outperformed bulk MnO_2, most likely due to the greater effect of the enhanced surface area on the catalytic activity than the crystal structure in this specific study. This means that both crystal structure and nanoscale morphology are important factors that determine the overall activity of oxygen electrocatalysts. In another work, Selvakumar *et al.* prepared α-MnO_2 having different nanoscale

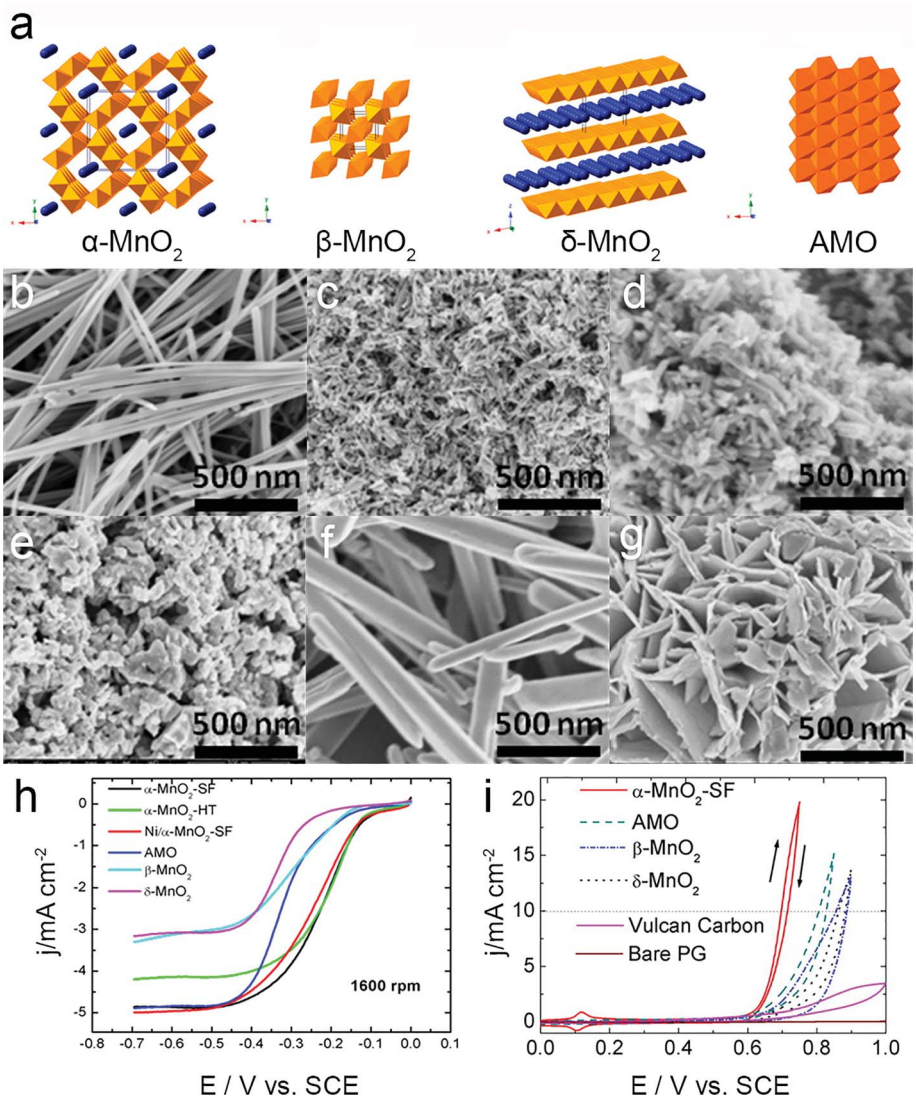

Fig. 3 (a) Various crystal phases of manganese oxide. SEM images of manganese oxide nanostructures: (b) α-MnO_2-HT (hydrothermal synthesis) (c) α-MnO_2-SF (solvent-free synthesis) (d) Ni-doped α-MnO_2-HT (solvent-free synthesis) (e) AMO (amorphous) (f) β-MnO_2 and (g) δ-MnO_2, (h) ORR, and (i) OER polarization curves of MnO_2 nanostructures obtained at 1600 rpm with a scan rate of 5 mV s^{-1} in O_2-saturated 0.1 M KOH solution.

morphologies: nanowires, nanotubes, and nanoparticles. According to their results, α-MnO_2 nanowires again demonstrated enhanced electrocatalytic activity compared to the other two nanostructures.[29]

Another interesting single metal oxide, Magneli phase Ti_4O_7, was investigated as an effective bi-functional catalyst in alkaline media.[24] The onset potentials of −0.02 and 0.74 V (*vs.* reversible hydrogen electrode (RHE)) were observed for ORR and OER in 6.0 M KOH, respectively, resulting in a narrow ORR and OER onset potential gap of 0.76 V. Remarkably, this Ti_4O_7 lasted 5000 cycles of CV in the potential range of −0.6 to 0.8 V (*vs.* RHE) without a significant activity loss, suggesting that it can be an active and durable bi-functional electrode material for rechargeable metal–air batteries.

3.2 Spinel type metal oxides

Spinel type metal oxides are one of the most popular bi-functional metal-based catalysts in the literature due to their simple synthetic routes, morphological flexibility and stability. Among the spinel type metal oxides, Co_3O_4 and other Co-based catalysts are the most investigated ORR and OER materials. Similar to manganese oxides, the capability of cobalt ions to exist in different valences leads to bi-functionality towards both OER and ORR by acting as donor–acceptor chemisorption sites for reversible adsorption–desorption of oxygen.[42] In a typical Co_3O_4 spinel structure, Co^{II} and Co^{III} states occupy the tetrahedral sites and octahedral sites, respectively. The tetrahedral Co^{II} ions are known to be the active sites for the ORR,[43] whereas the octahedral Co^{III} ions forming Co–O cubane units with O atoms are known to be the active sites for OER. During OER, cyclic voltammograms of Co surfaces show an anodic peak at ~550 mV (*vs.* Hg/HgO reference) prior to the onset of oxygen evolution, which is assigned to the oxidation of Co^{III} to Co^{IV}, and suggests that Co^{IV} centers are required to catalyze OER.[44,45] Koninck *et al.* studied this experimentally by substituting Co^{III} ions in Co_3O_4 with manganese ions, and observed that the intrinsic OER activity had decreased.[46,47] More recently, Menezes *et al.* found that the decrease in Co^{III} ions at the octahedral sites has a negative effect on oxygen evolution, while Mn at both tetrahedral and octahedral sites could be beneficial for ORR.[48] These studies allow researchers to engineer the composition of spinel oxides to fine tune the balance between the activities of ORR and OER to obtain an optimal bi-functional catalyst. Depending on the composition of spinel oxide catalysts, single (A_3O_4), binary ($A_xB_{3-x}O_4$), and ternary ($A_xB_yC_{3-x-y}O_4$) types of bi-functionally active catalysts are discussed in the following sections.

3.2.1 A_3O_4 type single metal oxides. Among many spinel type catalysts, Co_3O_4 has received much attention as an effective ORR/OER bi-functional catalyst due to its high activity and durability.[49–51] For instance, Sa *et al.* used mesoporous silica (KIT-6) as a template to obtain mesoporous Co_3O_4 structures, which demonstrated high bi-functional activity towards ORR and OER with high methanol tolerance.[50] Additionally, enhanced electrochemical durability of mesoporous Co_3O_4 was observed upon CV cycling between 1.25 and 1.65 V (*vs.* RHE) at 200 mV s^{-1} for 1500 cycles. Taking advantage of the electrochemical properties and stability of spinel Co_3O_4, Lee *et al.* synthesized morphologically controlled two-dimensional nanodisks with surface porosity. Upon electrocatalytic activity evaluation as a bi-functional air electrode material in a rechargeable zinc–air battery, superior galvanodynamic charge and discharge voltages were obtained compared to randomly shaped Co_3O_4 nanoparticles. Additionally, the nanodisks showed comparable discharge voltages to precious metal Pt/C catalysts, and virtually no voltage fading was observed over 60 pulse cycles.[52] Based on these studies, relatively simple compositions of single metal spinel oxides having unique nanostructures are observed to demonstrate sufficiently high activity for bi-functional oxygen electrocatalysis.

3.2.2 $A_xB_{3-x}O_4$ type binary metal oxides. The flexibility of spinel type oxides is highlighted by their lattices that are able to host different species of transition metals, resulting in a vast diversity of spinel oxide base catalysts reported in the literature. For example, depending on the type of substituent metal, $LiCoO_2$,[53,54] $Mn_xCo_{3-x}O_4$,[48,55–61] $Ni_xCo_{3-x}O_4$,[58,60,62–66] $Cu_xCo_{3-x}O_4$,[58,67–69] and $Zn_xCo_{3-x}O_4$ (ref. 58, 60 and 70) spinel oxides have been reported as efficient bi-functional air electrode materials. Typically, the compositions of simple single metal spinel oxides are modified with a second metal cation to fine tune properties such as crystalline structures and electrical conductivity that play important roles in oxygen catalysis. Many reports have been published on mixed-metal spinel oxides for bi-functional oxygen catalysis, particularly utilizing Co_3O_4 as the basis for compositional modification due to its high catalytic activity and valence stability as mentioned in the above section. In this section, bi-functionally active oxygen catalysts with the focus on Co_3O_4 partially substituted with other metallic cations are discussed.

In the work presented by Cheng *et al.*, two nanocrystalline $Co_xMn_{3-x}O_4$ spinels, CoMnO-P (coexistence of a major cubic spinel phase and a minor monoclinic birnessite phase) and CoMnO-B (tetragonal phase), were reported to be synthesized at room temperature through the reduction–recrystallization route using NaH_2PO_2 and $NaBH_4$ as reductants, respectively. Typically, the crystallographic phases of cobalt manganese oxides ($Co_{3-x}Mn_xO_4$) are sensitively determined by the Co/Mn ratio; namely, high Mn content ($1.9 \leq x \leq 3$) results in the tetragonal phase, while low Mn content ($0 \leq x \leq 1.3$) leads to the formation of the cubic spinel at room temperature. These two phases demonstrated higher performance than tetragonal $CoMn_2O_4$ and cubic Co_2MnO_4 powders synthesized by the traditional high-temperature method for both ORR and OER. This is largely attributed to the higher specific surface areas of nanocrystalline spinels providing more active sites for heterogeneous oxygen catalysis. Upon further analysis by density functional theory (DFT) calculations, the authors found that the cubic (113) surface generated much more stable molecular oxygen adducts than the tetragonal (121) surface, which is more favorable for ORR. Furthermore, for a given surface area, the number of available ORR active sites on the cubic (113) surface was found to exceed that on the tetragonal (121) surface. These

two reasons resulted in a superior ORR activity of CoMnO-P. However, CoMnO-B demonstrated more favorable OER activity, most likely because the processes involved are the reverse of ORR.

Another advantage of spinel oxides is the flexibility of synthesis methods used to produce them. Recently, Prabu *et al.* employed a simple electrospinning technique to prepare one-dimensional $NiCo_2O_4$ nanostructures (Fig. 4a).[63] Furthermore, the porous tubular and rod-like morphologies of $NiCo_2O_4$ could be obtained simply by adjusting the electrospinning parameters (Fig. 4b). The optimal $NiCo_2O_4$ structure was confirmed to be composed of ultrafine crystallite particles that formed a connective framework of nanotubes and nanorods (Fig. 4c and d). This specific structure led to the ORR and OER onset potentials of 0.78 V and 1.62 V (*vs.* RHE), respectively, resulting in the observed overpotential gap of 0.84 V (Fig. 4e). This was found to be smaller than the overpotentials of precious metal catalysts such as Pt/C (1.16 V), Ru/C (1.01 V) and Ir/C (0.92 V). When tested in a rechargeable zinc–air battery, the $NiCo_2O_4$ bi-functional air electrode demonstrated 1.8 and 1.1 V charge and discharge voltages *versus* zinc, respectively, at 20 mA cm^{-2} with only a 0.14 V increase in the charge–discharge gap over 50 cycles

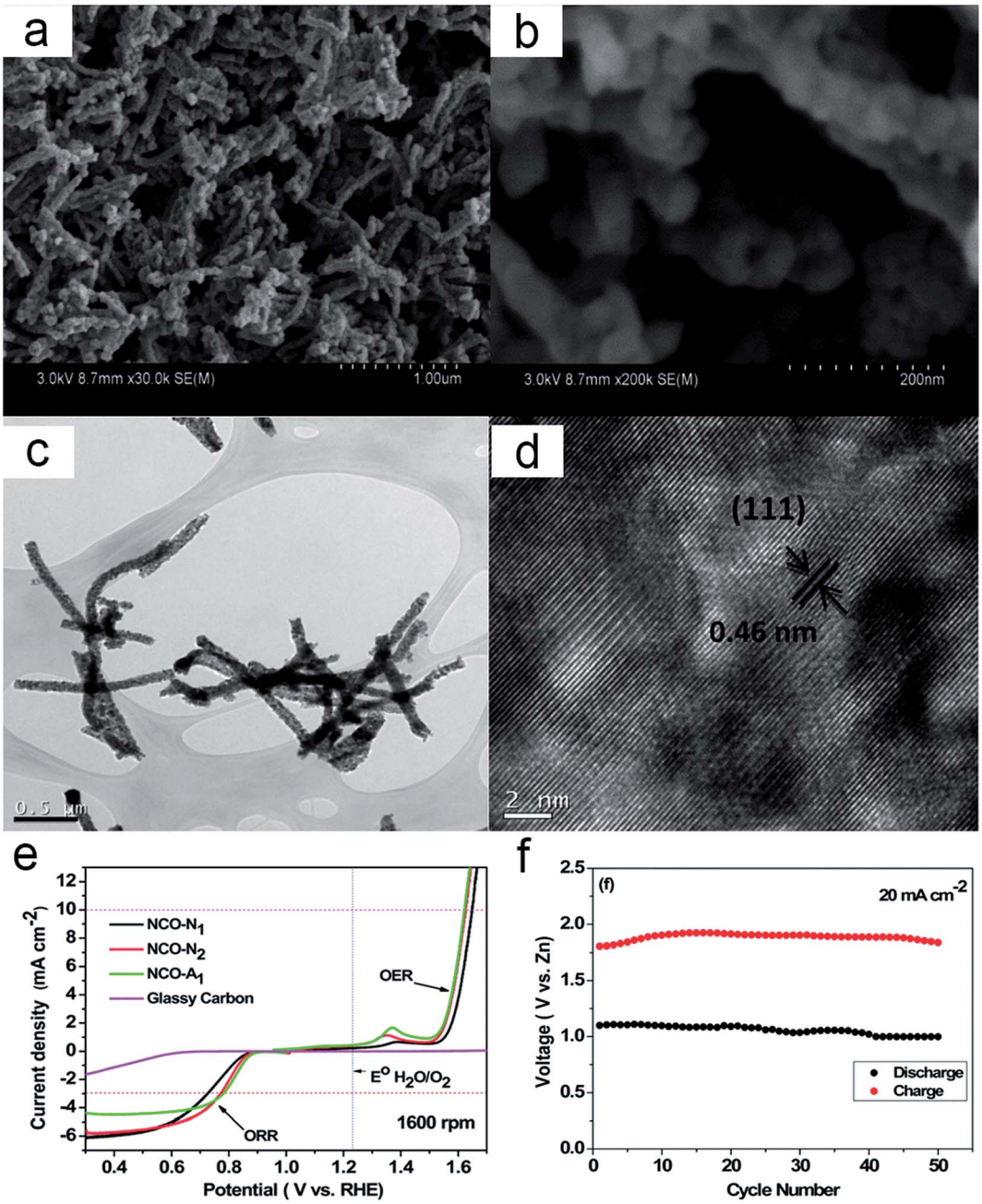

Fig. 4 (a and b) SEM images of NCO-A_1 (c and d) TEM and HTEM images of NCO-A_1 (e) ORR and OER activities of 1D NCO-N_1, NCO-N_2, and NCO-A_1 obtained at a rotation rate of 1600 rpm (f) Zinc–air battery charge and discharge voltages of NCO-A_1 obtained at the end of each state over 50 cycles (20 min for each state).

(Fig. 4f). In another study, well-ordered $NiCo_2O_4$ spinel nanowire arrays were synthesized by a facile template-free co-precipitation method. The nanowire arrays were found to have a mesoporous structure with a high specific surface area of 124 $m^2\ g^{-1}$, which resulted in highly promising ORR and OER bi-functional catalytic activity.[62]

3.2.3 $A_xB_yC_{3-x-y}O_4$ type ternary metal oxides. In ternary $A_xB_yC_{3-x-y}O_4$ type spinel oxides, three different cations coexist in the crystal, which makes it challenging to maintain the structure and control the parameters that affect the properties of materials and the resulting bi-functional catalytic activity. Regardless, there are a few reports in the literature on ternary spinel oxides that show bi-functionality towards the ORR and OER reactions.[31,47,71] For example, $Cu_xMn_{0.9-x}Co_{2.1}O_4$ nanoparticles were reported to be efficient bi-functional oxygen electrode materials and their activity was demonstrated in a regenerative fuel cell. Compared to the Pt/C electrode, the $Cu_xMn_{0.9-x}Co_{2.1}O_4$ modified air electrode exhibited ORR and OER activities with 50 mV and 100 mV improvements in terms of ORR half-wave potential and OER onset potential, respectively, in 1.0 M KOH.[31] In another report, the bi-functional catalytic activity of $Mn_xCu_{1-x}Co_2O_4$ $(0 \leq x \leq 1)$ was investigated, where both the ORR and OER were observed to be strongly dependent on the amount of Mn. Based on their results, $Mn_{0.6}Cu_{0.4}Co_2O_4$ was found to be a promising bi-functional air electrode material as Mn significantly enhanced the powder surface area, which in turn increased the geometric electrocatalytic activity. Despite the complexity of ternary spinel oxides, future research efforts in understanding the interactive roles of each cation will enable fine tuning and further optimization of bi-functional catalytic activity.

3.3 Perovskite-type metal oxides

Another group of materials characterized by their perovskite crystal structure with the general formula ABO_3, where A is a rare-earth metal or alkali-earth metal and B is a transition metal, are popular forms of bi-functionally active oxygen catalysts. Very complex perovskite oxides can be formed by partially substituting A and B with other rare-earth or alkali-earth metal and transition metal elements, respectively. Depending on the modification of their composition, perovskite oxides can be distorted from the basic cubic crystal structure, giving rise to a wide range of electrochemical properties. The bi-functional ORR/OER activity of perovskites mainly comes from the flexibility of the transition metal ions. This allows the formation of

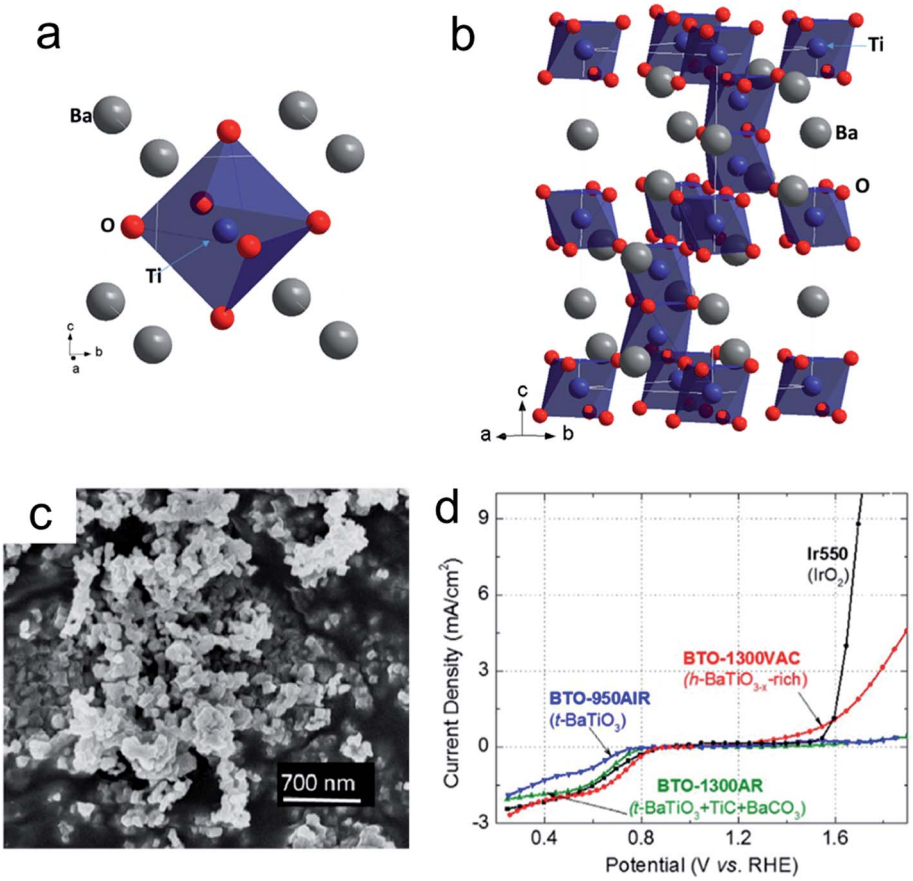

Fig. 5 A unit cell of the crystal structures of (a) tetragonal $BaTiO_3$ and (b) hexagonal $BaTiO_3$. Gray spheres represent Ba, blue spheres represent Ti, and red spheres represent O. The O sites are partially occupied in the hexagonal structure. (c) SEM image of BTO-1300VAC (heat treated at 1300 °C in vacuum). (d) ORR and OER polarization curves of Ir-550, BTO-950AIR, BTO-1300AR, and BTO-1300VAC obtained at a rotation rate of 900 rpm in 0.1 M NaOH electrolyte at 25 °C.

redox couples and defects *via* oxygen vacancies or excess, which result in excellent oxygen anion mobility, and exchange kinetics.[72] The active site of the electrocatalytic oxygen reactions on perovskite oxide surfaces is generally regarded as the B site cation. For instance, the B site Co and Mn cations are known in the literature to be effective in catalyzing the oxygen reactions.[73–75] In particular for OER, Suntivich *et al.*[76] suggested, based on the study of e_g orbital filling, that the optimum bond strength between the catalyst and reaction intermediates leads to maximized catalytic activity. The ORR, on the other hand, is generally known to be relatively weak on perovskite oxides due to the formation of both OH^- and HO^{2-}, resulting in a 2- and 4-electron mixed control process.[76] Although uncertainties still remain in terms of the exact ORR and OER mechanisms on the perovskite surface, researchers have been improving the oxygen catalytic activity through improving redox couples, oxygen mobility and electrical conductivity based on flexible modification of perovskite oxide cations. So far, researchers have developed several different types of perovskites including binary perovskites including BaTiO,[78] and LaMO (M = Mn,[79,80] Fe,[79] Co,[79] Ni[79,81–84]), ternary perovskites including LaCaMnO,[85] LaCaCoO,[86–90] LaSrMnO,[91] LaSrFeO,[92] LaSrCoO,[93–97] and LaNiMO (M = Fe,[98] Mn),[79] quaternary perovskites including BaSrCoFeO,[80,99–101] BaCoFeNbO,[102] LaSrCoFeO,[103] LaCaFeMnO,[103] and LaSrCoFeO[103] in addition to even more complex oxides containing five different cations such as LaNaSrCoFeO.[104] Bi-functionally active ORR and OER catalysts based on these various perovskite structures are discussed in the following sections.

3.3.1 Binary perovskite oxide. Shao-Horn and co-workers have conducted abundant research on perovskite type oxygen catalysts including bi-functionally active ORR/OER[80,105–107] catalysts. Jung *et al.*[104] prepared $La_{0.3}(Ba_{0.5}Sr_{0.5})_{0.7}Co_{0.8}Fe_{0.2}O_{3-\delta}$ with 10 nm-scale rhombohedral $LaCoO_3$ cobaltite particles distributed on its surface, showing ORR and OER activity competitive with those of conventional RuO_2 and IrO_2 precious metal-based catalysts. The degree of electrochemical oxygen catalysis on perovskite oxides is known to largely vary with the characteristics of the surface cation which in turn is determined by the level of oxygen atom deficiency in the oxide. In this regard, Chen *et al.* introduced a unique oxygen-deficient hexagonal $BaTiO_{3-x}$ crystal structure (h-$BaTiO_{3-x}$) synthesized by a sol–gel method, followed by a heat treatment at 1300 °C under vacuum.[78] Compared to tetragonal $BaTiO_3$ produced by heat treatment at 900 °C in air (t-$BaTiO_3$) (Fig. 5a), h-$BaTiO_{3-x}$ is characterized by partially occupied oxygen sites (Fig. 5b). The oxygen-deficient h-$BaTiO_{3-x}$ was observed to be composed of nanoparticles with an average particle size of 110 nm (Fig. 5c). In comparison to t-$BaTiO_3$ and an additional sample heat treated at 1300 °C in argon which was found to consist of a mix of t-$BaTiO_3$, TiC and $BaCO_3$, the oxygen-deficient h-$BaTiO_{3-x}$ demonstrated a superior bi-functional oxygen electrocatalytic activity, particularly for OER which outperformed precious metal benchmark IrO_2 at potentials lower than 1.6 V (*vs.* RHE) in terms of current density generated (Fig. 5d). Neutron analysis revealed the actual chemical formula of the oxygen-deficient h-$BaTiO_{3-x}$ to be $BaTiO_{2.76}$ and the bi-functional catalytic activity was attributed to the oxygen vacancies in $BaTiO_{2.76}$ facilitating reactant-adsorption and charge transfer. This highlights the importance of structures and oxygen content of perovskite oxides which can be controlled by heat treatment temperature and atmosphere parameters.

3.3.2 Ternary perovskite oxide. Takeguchi and co-workers[92] reported Ruddlesden–Popper-type layered perovskite oxide (RP-$LaSr_3Fe_3O_{10}$) as a bi-functional air electrode material for rechargeable metal–air batteries. Because of the easily removable oxygen in RP-$LaSr_3Fe_3O_{10}$, it almost functions as a reversible air electrode catalyst for both ORR and OER at an equilibrium potential of 1.23 V. Later, another group synthesized cation-doped lanthanum nickelates also having a layered perovskite structure as bi-functional oxygen electrocatalysts.[82] The best performing ORR and OER catalyst, $La_{1.7}Sr_{0.3}NiO_4$ (LSN-03), was tested as a cathode in lithium–air and zinc–air batteries. In the lithium–air battery, the voltage gap between discharging and charging at 2.0 mA cm^{-2} was as small as 1.16 V with LSN-03 (550 mV reduction compared to a catalyst-free battery). When LSN-03 was employed as a cathode catalyst in a zinc–air battery, the voltage gap (~1.51 V) at 75 mA cm^{-2} was smaller than that for Pt/C (~1.62 V) and decreased by 380 mV relative to a catalyst free battery.

3.3.3 Quaternary perovskite oxide. Jin *et al.*[100] prepared $Ba_{0.5}Sr_{0.5}Co_{0.8}Fe_{0.2}O_3$ (BSCF) perovskite oxide by a sol–gel method followed by calcination in air at 900 °C. The as-obtained catalyst was supported by carbon and tested for ORR and OER activity in 0.1 M KOH. With rotating ring-disk electrode (RRDE) testing, the BSCF showed a direct four electron pathway and a maximum cathodic current density of 6.25 mA cm^{-2} at 2500 rpm, approaching that of the commercial 20% Pt/C catalyst tested under the same conditions. Also, the onset potential of the BSCF catalyst positively shifted to 0.12 V as compared to pure carbon, demonstrating the ORR function of BSCF. In the OER region, the onset potential of the BSCF catalyst is 0.2 V lower than that of pure C, demonstrating the BSCF catalyst to be an encouraging catalyst for OER. In their later work, a perovskite with another formula $Ba_{0.9}Co_{0.5}Fe_{0.4}Nb_{0.1}O_3$ (BCFN) was prepared and applied in a lithium–air battery, which demonstrated a maximum discharge capacity of 1235 mA h g^{-1} electrode at 50 mA g^{-1}.

3.4 Other transition metal-based compounds

Due to the flexibility of the synthesis of transition metal-based oxides, there are many more types other than spinel and perovskite oxides such as amorphous metal oxides that show considerable bi-functional activity towards oxygen electrochemical reactions. Other active air electrode materials apart from transition metal oxides such as doped metal oxide,[108] transition metal alloys,[109] hydroxides,[110] nitride[111,112] and sulfides[113,114] have also been reported recently as active bi-functionally electrocatalytic materials for ORR and OER. For example, Indra and co-workers[115] synthesized crystalline $CoFe_2O_4$ (CIO-1) and amorphous $CoFe_2O_n$ ($n \sim 3.66$) (CIO-2) by controlling the crystallinity of the oxides by using different solvents and reaction times. The half-cell electrochemical evaluation revealed that amorphous oxide outperformed the

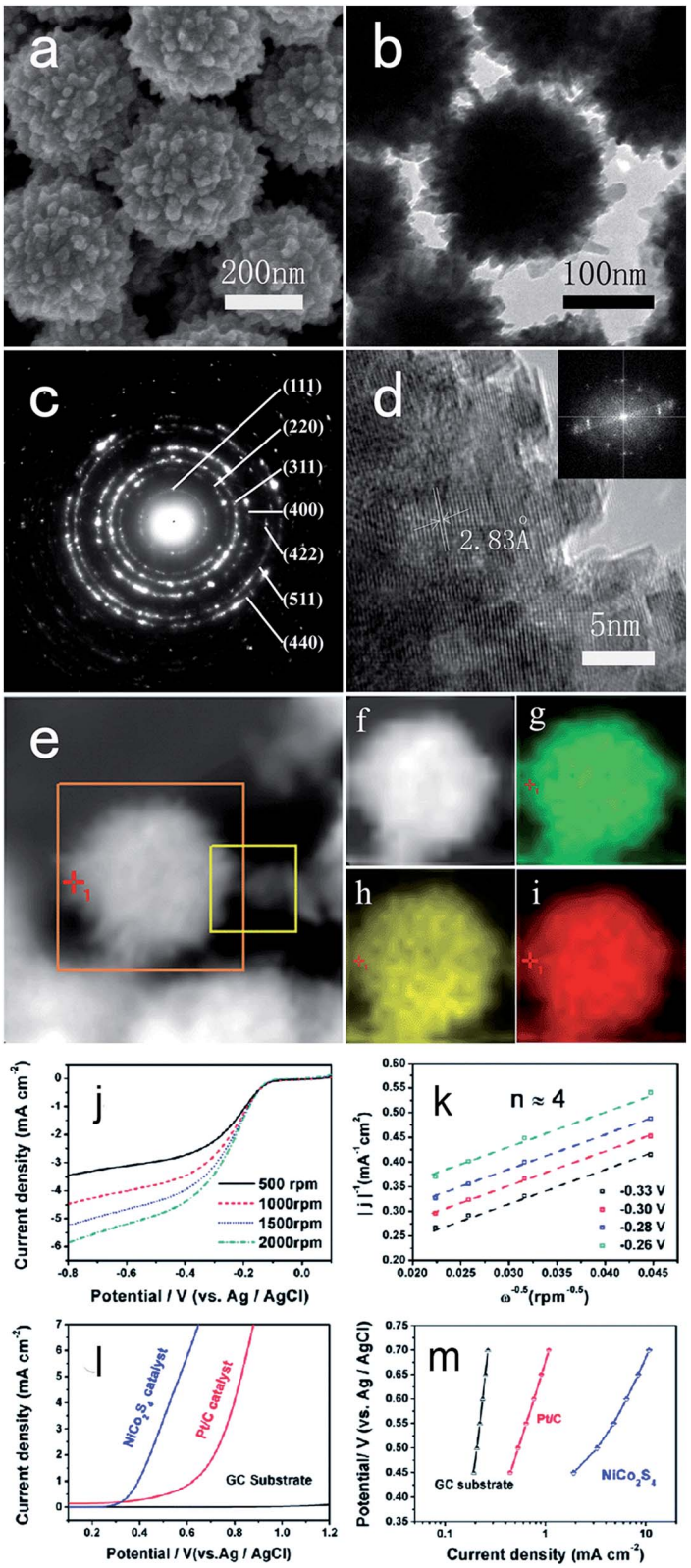

Fig. 6 (a) SEM, and (b) TEM images of $NiCo_2S_4$ SMS. (c) SAED pattern of a single $NiCo_2S_4$ SMS. (d) HRTEM image of a typical nano-papillae surface of $NiCo_2S_4$ SMS. Inset: the corresponding SAED pattern. (e) Typical STEM image of $NiCo_2S_4$ SMS. (f) STEM image taken from the square region marked in (e). (g–i) The corresponding elemental mapping images of (g) Ni, (h) Co and (i) S. (j) LSV curves of $NiCo_2S_4$ SMS in an O_2-saturated 0.1 M KOH electrolyte obtained at different rotation rates with a sweep rate of 10 mV s^{-1}. (k) Corresponding Koutecky–Levich plots (j^{-1} *vs.* $\omega^{-0.5}$) obtained at different potentials from (j) LSV curves. (l) OER polarization curves, and of $NiCo_2S_4$ SMS, Pt/C, and GC substrate obtained at a sweep rate of 10 mV s^{-1} in 0.1 M KOH electrolyte. (m) Corresponding OER Tafel plot of $NiCo_2S_4$ SMS, Pt/C, and GC substrate.

crystalline counterpart in terms of facilitating both ORR and OER. After characterization by X-ray absorption spectroscopy (XAS), amorphous CIO-2 was found to contain more Co^{3+} than crystalline $CoFe_2O_4$. It was also confirmed by temperature programed reduction (TPR) that amorphous CIO-2 had more reducible sites than crystalline $CoFe_2O_4$. The better OER performance of amorphous $CoFe_2O_n$ could be explained by the combination of the higher surface area and the presence of the higher content of Co^{3+} in the octahedral sites. For ORR, CIO-2 showed significantly higher ORR activity compared to CIO-1. On the basis of the K–L plot, the electron transfer number of CIO-2 is close to 4, reflecting direct reduction of molecular O_2 to H_2O.

Rafailović *et al.*[109] reported the synthesis of a porous NiCoFe foam by electrodeposition. Ternary NiCoFe alloys were deposited at different current densities, where a smooth electrode and a multiscaled 3-dimensional (3D) porous dendritic structure NiCoFe foam were obtained at current densities of 0.1 A cm^{-2} and 1 A cm^{-2}, respectively. Compared to the smooth electrode, the porous electrode demonstrated higher activity in terms of both ORR and OER due to the 3D morphology leading to a higher surface area and a higher density of active sites (defects). Wang *et al.*[110] reported the synthesis of transition metal-based hydroxide catalyst $Ni_xCo_{1-x}(OH)_2$ with different compositions and morphologies as a bi-functionally active material. Both multi-layer and single-layer $Ni(OH)_2$ demonstrated superior OER activities compared with $Co(OH)_2$ and $Ni_{0.55}Co_{0.45}(OH)_2$. For ORR, both multi-layer and single-layer $Co(OH)_2$ exhibited better catalytic activities than $Ni(OH)_2$ and $Ni_{0.55}Co_{0.45}(OH)_2$. It was also observed that single layer catalysts are generally superior in terms of both ORR and OER. Namely, in this paper, single-layer $Ni(OH)_2$ and $Co(OH)_2$ were the best performing catalysts for OER and ORR, respectively. As a transition metal nitride based catalyst, titanium nitride nanoparticles supported on carbon black Vulcan XC-72 (n-TiN/VC) were reported as an efficient ORR and OER catalyst for lithium–air batteries by Li and co-workers.[111] The discharge–recharge voltage gap of n-TiN/VC was estimated to be 1.05 V, which was 390 and 450 mV smaller than that of a mixture of micro-sized TiN and VC (m-TiN/VC), and VC, respectively, at 50 mA per g carbon. The enhanced performance was ascribed to the combination of the intrinsic high catalytic activity of TiN and the improved contact between TiN and VC prepared *via* the template method.

Transition metal sulfides are a relatively new type of material in the field of bi-functional oxygen catalysis. Only a few reports on bi-functional oxygen catalysis are available in the literature, but they are important for introducing the possibility of a new class of materials to the oxygen catalyst research community. Among them, Zhang *et al.* have reported urchin-like $NiCo_2S_4$ sub-micron spheres (SMS) made up of smaller nano-sized structures synthesized by a facile one-pot method.[113] $NiCo_2S_4$ SMS were characterized by SEM (Fig. 6a) and TEM (Fig. 6b) to show uniform spherical structures with an average diameter of 0.25 μm decorated with nano-papillae particles. The ring patterns revealed by selected area electron diffraction (SAED) (Fig. 6c) characterizing the nano-papillae particles observed in the high-resolution TEM image (Fig. 6d) demonstrated a well-defined crystal structure of $NiCo_2S_4$ SMS. In addition, the elemental mapping of an individual sphere (Fig. 6e and f) revealed that Ni (Fig. 6g), Co (Fig. 6h), and S (Fig. 6i) atoms were uniformly distributed throughout the sphere. Upon half-cell RDE electrochemical evaluation, the ORR polarization curves obtained with $NiCo_2S_4$ SMS at various rotation speeds in 0.1 M KOH (Fig. 6j) resulted in first-order dependent O_2 kinetics with 3.98 electrons transferred per O_2 molecule based on Koutecky–Levich analysis (Fig. 6k). The OER curve of $NiCo_2S_4$ SMS showed significantly improved activity compared to Pt/C (Fig. 6l), with superior reaction kinetics as demonstrated by the Tafel analysis (Fig. 6m). The bi-functional activity of $NiCo_2S_4$ SMS was attributed to the unique d-electronic configuration of the surface Co^{III} cation resulting from sulfur vacancies. Based on the results of this work, future investigations on metal sulfides can further optimize sulfur vacancies, similar to oxygen vacancy investigations of metal oxides to render highly active bi-functional catalysts.

3.5 Transition metal-based hybrids

As the last section of transition metal-based catalysts, examples of hybridized transition metal hybrids are introduced as bi-functional catalysts. These have not been commonly reported in the literature, but they open new directions for research to develop cost-effective and active catalysts. The hybridized catalysts take advantage of specific properties from each component to optimize the catalytic ORR and OER activity.[26,71,116–125] For example, Shao-horn and co-workers[122] reported $La_{0.8}Sr_{0.2}MnO_{3-\delta}$ (LSMO) decorated with $Ba_{0.5}Sr_{0.5}Co_{0.8}Fe_{0.2}O_{3-\delta}$ (BSCF) by the pulsed laser deposition method to fabricate well-defined surfaces composed of BSCF on thin film LSMO grown on (001)-oriented Nb-doped $SrTiO_3$. Since LSMO and BSCF are known to demonstrate high intrinsic ORR and OER activities, respectively, the combination of the two is reasonable to obtain a highly active bi-functional catalyst. As such, the catalyst demonstrated the lowest state-of-the-art overpotential gap of 0.7 V for OER current density at 100 μA/cm_{ox}^2 and absolute ORR current density at 20 μA/cm_{ox}^2. Similarly, Du *et al.* reported hybridization of spinel oxides in the form of Co_3O_4 nanoparticle-modified MnO_2 nanotubes and their application as bi-functional cathode catalysts for zinc–air batteries.[118] The hybrid material shows enhanced activity as compared to MnO_2 nanotubes and CoO_4 nanoparticles alone due to the synergistic effect and interface effect between the two components. Herein, Co_3O_4 nanoparticles and MnO_2 nanotubes are believed to offer high performance for the OER and ORR, respectively.

4. Carbon-based materials

Carbon based materials, particularly hetero-atom doped graphitized carbons such as graphene nanosheets and carbon nanotubes, have been widely investigated as active ORR catalysts. Through hetero-atom doping, the catalytic activity of carbon-based bi-functional catalysts is significantly improved due to the changes in the electronic structure of the carbon

species as well as defects that act as the ORR active sites.[126] Unlike ORR, the investigation of OER on carbon surfaces is still in its early research stage, hence the adsorption–desorption behaviors of oxygen species and the exact reaction mechanism during OER are not clear, but are topics of continuous research. Besides, their application in OER has been limited by their electrochemical instability at relatively high potentials. However, with continuous advancements in carbon based catalyst developments, publications are emerging in this relatively new field of research.

4.1 M–N/C complexes

Transition metal and nitrogen co-doped carbon materials, namely M–N/C (M = transition metal, N = nitrogen, C = carbon) materials are well-known non-precious ORR catalysts.[127–132] An atomically dispersed iron–nitrogen–carbon (Fe/N/C) composite and its catalytic performance were first evaluated for lithium–air battery application.[129] The Fe/N/C catalyst significantly outperformed the well-known benchmark α-MnO_2 in Li–O_2 cell tests. Sun *et al.*[130] reported organic-electrolyte-dissolved iron phthalocyanine (FePc) as a solution phase bi-functional catalyst for lithium–air batteries. In the proposed ORR and OER mechanism, FePc served as a shuttle of O_2^- species and electrons between the surface of the carbon electronic conductor and Li_2O_2 sites. Because Li_2O_2 grew and decomposed without direct contact with carbon, electrochemical performance was greatly enhanced.

4.2 Metal free carbon materials

Metal free carbon materials have been studied extensively for the ORR during the last decade primarily for fuel-cell applications. However, they have not been readily employed as bi-functionally active catalysts due to the corrosion of carbon at high OER potentials which leads to electrocatalytic activity degradation. Unlike other carbons, however, graphitic structures such as graphene nanosheets and carbon nanotubes are made of carbon bonds that are much tightly packed and are sp^2 orbital hybridized, rendering them electrochemically much more stable.[133,134] As such, reports on the bi-functional catalytic activity of carbon materials deal with graphitic carbons such as graphene[135–145] and carbon nanotubes (CNT).[146–152] Heteroatom doped graphene and CNT show high ORR/OER activities rendering them sufficiently active and durable for rechargeable metal–air batteries. Still, other carbon based bi-functional catalysts are reported in the literature such as carbon black,[153] mesoporous noble carbon,[154] hierarchical mesoporous/macroporous carbon,[155] N-doped porous carbon,[156] and nitrogen and phosphorus co-doped mesoporous carbon foam,[157] which are usually more advantageous in terms of a facile synthesis process and lower materials cost. The following sections discuss recent reports on bi-functional catalysts based on graphitized carbons and other types of carbon based materials.

4.2.1 Graphene based materials. As mentioned above, carbon corrosion at high potentials usually incurred during OER (charging) is inevitable for conventional electrodes. However, the excellent electrochemical stability of graphene allows for its use in bi-functional catalyst applications usually with the help of properly introduced heteroatom dopants. For instance, a few-layer nanoporous nitrogen-doped graphene (NG) was prepared by a simple pyrolysis of graphene and polyaniline, and was used as an efficient electrocatalyst for bi-functional oxygen catalysis.[137] The NG showed excellent ORR activity (onset potential of 0.08 V *vs.* RHE), and long-term stability (minimal change was observed in the CV curve of NG-900 after 2000 CV cycles in the oxygen saturated 0.1 M KOH) as well as good tolerance to methanol in alkaline media. Simultaneously, the high OER activity of NG was also demonstrated (superior to that of the commercial Pt/C catalyst), rendering its potential application for rechargeable metal–air batteries. In another publication by the same group, a similar result was obtained using polypyrrole as the nitrogen dopant source instead of polyaniline. More compositionally complex graphene based catalysts with two dopants were reported by Li *et al.*, demonstrating a cost effective strategy to fabricate nitrogen and phosphorus dual-doped graphene/carbon nanosheets (N,P-GCNS) with hierarchically porous sandwich-like structure.[136] N,P-GCNS demonstrated an excellent potential gap of 0.71 V between OER at 10 mA cm^{-2} and ORR at -3 mA cm^{-2}. While the high catalytic activity of N,P-GCNS is ascribed to the synergistic effects of N and P atoms that effectively facilitate both ORR and OER, many of the advantages also stem from the intrinsic properties of graphene nanosheets such as large surface areas for enhanced active site exposure, high electrical conductivity for rapid charge transfer and porous inter-particle architecture for improved mass transportation. These qualities of graphene based materials which are highly suited for electrochemical oxygen reactions, in addition to their relatively cheaper price, need to be exploited rigorously in future catalyst research.

4.2.2 Carbon nanotube based materials. Tian *et al.* reported CNT@NCNT coaxial nanocables as an efficient metal-free nanocarbon electrocatalyst which has surface enriched nitrogen species for facilitating oxygen reduction and evolution reactions.[148] Carbon nanotubes having very high surface areas were chosen as the platform to demonstrate the potential of full exposure of 'active sites' at the surface. The unique design of CNT@NCNT coaxial nanocable catalysts afforded both highly active reaction sites and an electrically conductive backbone through accessible and efficient utilization of the integrated N atoms enriched on the surface and the intact undestroyed inner walls, respectively. TEM analysis was conducted to compare morphological differences between pristine CNT (Fig. 7a), NCNT (Fig. 7b), and CNT@NCNT coaxial nanocables (Fig. 7c). Unlike the typical bamboo-like microstructure of NCNT, CNT@NCNT nanocables showed a tubular morphology. In fact, the nanocable consisted of a N-doped wrinkled carbon layer epitaxially grown on the outer surface of the cylindrical CNT. This unique microstructure of CNT@NCNT having concentrated active sites on its surface showed reduced overpotentials of 51 mV for ORR (Fig. 7d) and 20 mV for OER (Fig. 7e) and higher current toward OER, making the CNT@NCNT coaxial nanocables a promising bi-functional electrocatalyst.

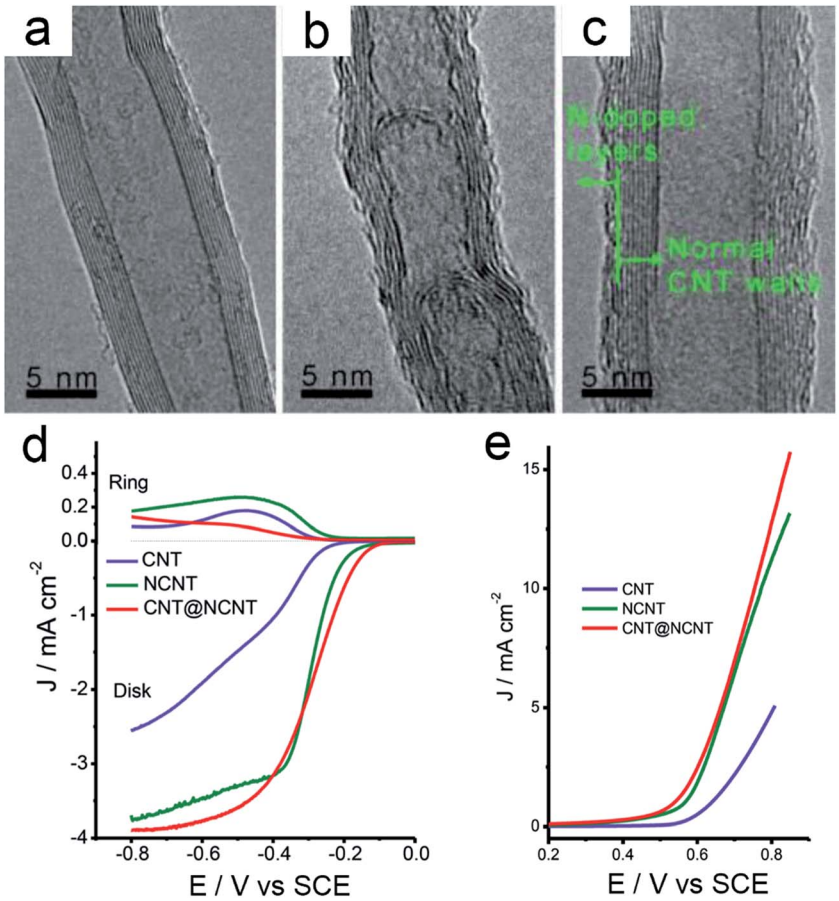

Fig. 7 TEM images of (a) pristine CNTs, (b) NCNTs, and (c) CNT@NCNT coaxial nanocables. (d) Rotating ring disk voltammograms recorded for CNT, NCNT, and CNT@NCNT electrode in an O_2-saturated 0.1 mol L^{-1} KOH solution at a scan rate of 5.0 mV s^{-1}. The disk current densities (bottom) and the corresponding ring current densities (top) are displayed separately as illustrated in the figure and the rotating speed of the electrode was 1600 rpm. (e) OER currents of the CNT, NCNT, and CNT@NCNT catalysts in 0.1 mol L^{-1} KOH solution at a scan rate of 5.0 mV s^{-1}.

Yadav *et al.*[149] also conducted rigorous investigation on carbon nanotube based catalysts using acetonitrile (ACN), dimethylformamide (DMF), trimethylamine (TEA) and hexamethylenetetramine (HMTA) as nitrogen containing precursors to control the diameters. In their work, bamboo-shaped carbon nitrogen nanotubes (CNNTs) with mean diameters varying from 20 to 66 nm were synthesized by using a liquid chemical vapor deposition technique. The activities of CNNTs are strongly dependent on the nanotube diameter and nitrogen functionality type. It was found that the higher diameter CNNTs were more favorable for the oxygen reactions. The CNNT-ACN with the largest diameter demonstrated both superior ORR and OER activity compared with the other three samples. The onset potential of CNNT-ACN for ORR (0.93 V *vs.* RHE) was 150 mV more positive than that of CNNT-HMTA (0.78 V *vs.* RHE). Regarding the OER, the CNNT-ACN reached 1.68 V *vs.* RHE at 10 mA cm^{-2}. The CNNT-ACN and CNNT-DMF catalysts both afforded much higher OER currents than the CNNT-TEA, CNNT-HTMA, and Pt/C catalysts (at high overpotentials). It can be concluded that the increase in nanotube diameter itself enhances the catalytic activity for both OER and ORR. This trend originates from the nitrogen moieties by lowering the oxygen adsorption energy and enhanced conductivity. Cheng *et al.* also studied the effect of carbon nanotube size and the number of nanotube walls on ORR and OER activity.[147] It was demonstrated that the catalytic performance of the metal free (residual metallic impurity-blocked) carbon nanotubes (CNTs) strongly depended on the number of walls or inner tubes. CNTs with 2–3 walls exhibited the most enhanced activity for both ORR and OER in this work. The intrinsic activity of CNTs was ascribed to the quantum properties of CNTs, namely, the significantly enhanced charge transfer *via* the electron tunnelling between the outer wall and inner tubes *via* electron tunnelling of CNTs under the electrochemical polarization potential driving force.

4.2.3 Other carbon materials. Other than graphitized carbon, publications are scarce due to the aforementioned issue of carbon corrosion during exposure to high potentials. Based on a few articles found in the literature, mesoporous nitrogen-doped noble carbons (meso-NdCs) were prepared using ionic liquid *N*-butyl-3-methylpyridinium dicyanamide as a nitrogen precursor and SiO_2 nanoparticles as a hard template for mesoporous control.[154] The as-synthesized material was found to demonstrate high bi-functional ORR/OER activity and oxidation stability. Interestingly, depending on the ionic liquid composition and the thermal treatment conditions used during the

synthesis, the catalytic selectivity of meso-NdCs was found to be very different. Meso-NdC with nitrogen contents of up to 12 wt% acted as an efficient bi-functional catalyst for both ORR and OER demonstrated using a lithium–air battery set-up. The high nitrogen content enabled charging of the battery at 3.41 V *vs.* Li/Li^+, significantly reducing the charge overpotential to as low as 0.45 V. The oxidation stability resulting from increased condensation and conjugation obtained by high temperature carbonization makes the reported noble carbon suitable for applications in rechargeable metal–air batteries. Zhang *et al.*[157] paired nitrogen and phosphorous co-doped mesoporous carbon (NPMCs) foam prepared simply by pyrolysing polyaniline aerogels obtained from polymerization of aniline in the presence of phytic acid. The resultant NPMCs have a large surface area of $\sim$1663 $m^2\ g^{-1}$ and outstanding catalytic properties for both ORR and OER as bi-functional air electrodes. Primary batteries demonstrated an open-circuit potential of 1.48 V and a peak power density of 55 mW cm^{-2}. For durability, two-electrode rechargeable batteries could be stably cycled for 180 cycles at 2 mA cm^{-2}. Furthermore, first-principles calculations were performed using DFT methods to determine the electronic structures and catalytic reactions for the N,P co-doped carbon structures. The minimum overpotentials of N,P co-doped graphene for ORR and OER were identified to be 0.44 V and 0.39 V respectively, lower than those of the best catalysts identified theoretically ($\sim$0.45 V for ORR on Pt and $\sim$0.42 V for OER on RuO_2), indicating that the N,P co-doped graphene material could outperform its noble metal/metal oxide counterparts.

4.2.4 Metal free carbon material hybrids. Research efforts have been devoted to the development of metal-free carbon hybrids,[158–161] which typically consist of two different types of carbon materials. For example, Tian and co-workers reported a new N-doped graphene/single-walled carbon nanotube hybrid (NGSH) as an efficient bi-functional electrocatalyst for improving ORR and OER.[159] NGSH bifunctional catalysts were synthesized by *in situ* doping during chemical vapor deposition growth on FeMoMgAl layered double hydroxide used as a growth catalyst. The one-step approach led to the formation of a three-dimensionally interconnected graphene and carbon nanotube network. Also, it brought good dispersion of graphene and carbon nanotubes and good distribution of N-containing active functional groups within a highly conductive scaffold even though the hybrid material possessed a low overall nitrogen content (0.53 at%). The catalyst demonstrated a high ORR activity comparable to that of commercial 20 wt% Pt with superior durability and cross-over resistance as well as a high OER activity (10 mA cm^{-2}@1.63 V *vs.* RHE) similar to that of IrO_2/C, which demonstrated it to be a high-performance cost effective bi-functional catalyst.

5. Hybrid materials

As mentioned in previous sections, transition metal species in general demonstrate high OER activity, but often lack ORR capabilities. Meanwhile, heteroatom-doped graphitic carbons are proven to be effective for ORR, but is susceptible to thermodynamic instability under the oxidative OER conditions. Therefore, researchers have developed ways to combine these two types of materials to form hybrid bi-functional catalysts, which often demonstrate synergistically enhanced ORR and OER activities. Typically, the carbon material either acts as an electrical conductive support, or as an active catalyst, or both. In the form of the former, a high surface area nanostructured carbon is usually employed to help the dispersion of metal oxide to facilitate charge transport of metal oxides that have intrinsically low electrical conductivity. In the form of the latter, the active carbon acts as an oxygen electrocatalyst to improve the activity of ORR, while the metal oxide facilitates OER. In this form, the synergy between carbon and metal oxide is often observed, resulting in higher ORR and OER activities together as a hybrid than the activities of the individual components. Such synergetic effects observed with hybrid catalysts are attributed to two factors: (i) the electronic interaction between carbon and metal species creates rapid electron transfer paths;[77,162] (ii) the active carbon species initially facilitate the reduction of O_2 to HO_2^-, and then the metal species subsequently catalyze HO_2^- to OH^-, resulting in the overall four-electron reduction process.[163] The following sections will introduce hybrid catalysts based on different compositions, morphologies and synthesis techniques.

5.1 Single metal oxide & carbon material hybrids

As previously discussed in Section 3.1, many single metal oxides have been studied as active bi-functional oxygen catalysts. This section introduces reports on the bi-functional activity of metal oxides combined with carbon materials. Based on the reports found in the literature, Mn oxide,[164–174] Fe oxide,[174–176] Co oxide,[167,177–180] Ni oxide,[174,181] Cu oxide[174] and Zn oxide[182] hybridized with graphene or CNT are discussed.

Liu *et al.* reported the fabrication of Co-CoO/N-GO and Ni-NiO/N-GO *via* a pyrolysis of GO and cobalt or nickel salts.[181] Based on the results of half-cell electrochemical tests, Ni-NiO/N-rGO presented the lowest overpotential of 0.24 V at a current density of 10 mA cm^{-2} for OER, which is much smaller than overpotentials measured with benchmark IrO_2 (0.33 V). For ORR, even though Co-CoO/N-rGO exhibited lower activity compared to Pt/C, it exhibited the highest electrocatalytic activity among the metal, metal oxides and N-rGO hybrids. However, the lower resistance and favorable mass transfer due to porous graphene cathode layers led to improved performance for the Co-based catalyst in rechargeable zinc–air batteries, which is even comparable to Pt/C + IrO_2 modified electrode in terms of OER and ORR potentialgaps.

The hybrid catalysts also exhibited high activity in non-aqueous organic electrolytes. For example, α-Fe_2O_3 nanoparticle *in situ*-decorated carbon nanotubes were demonstrated to be an efficient bi-functional air electrode material for rechargeable non-aqueous lithium–air batteries.[175] The CNTs were grown on stainless steel meshes followed by deposition of Fe nanoparticles to get Fe/C-CNT. Then, α-Fe_2O_3–CNT samples were obtained by annealing the as-grown Fe/C-CNT sample in air. Upon rechargeable lithium–air battery testing, α-Fe_2O_3 deposited CNTs demonstrated significantly enhanced formation of

Li_2O *via* the four-electron reduction pathway, in addition to Li_2O_2 commonly formed *via* the one/two-electron reduction pathway. Due to the favorable kinetic process, the lithium–air battery delivered a high specific capacity of 26.5 mA h g^{-1} and a relatively long cycling performance (48 cycles with a specific capacity limit of 1.5 mA h g^{-1}).

5.2 Spinel-type metal oxide & carbon material hybrids

Another hybrid type catalyst that is of great interest in bi-functional oxygen catalysis is a combination of spinel-type oxides with carbon materials. Compared to other types of metal oxide and carbon material hybrids, spinel and carbon hybrids have gained more attention from researchers due to the high OER activity of spinels complemented by the high ORR activity of carbon materials. In this section, spinels such as Co_3O_4,[163,183–191] MnCoO,[192–201] FeCoO,[202–206] NiCoO,[207,208] and MnFeO[205] hybridized with carbon materials are discussed.

Spinel Co_3O_4 crystals coupled with nitrogen-doped reduced graphene oxide (Co_3O_4/N-rmGO) for both ORR and OER were reported by Liang and co-workers.[163] Co_3O_4 crystals were grown on mildly oxidized GO sheets (mGO) by hydrolysis and oxidation of cobalt acetate, and NH_4OH was added during the hydrolysis process to introduce nitrogen dopants into reduced graphene oxide sheets. Physical characterizations of Co_3O_4/N-rmGO revealed that Co_3O_4 nanoparticles were evenly distributed on nitrogen-doped graphene oxide sheets. Based on ORR performance evaluation, Co_3O_4/N-rmGO was found to demonstrate the highest activity compared to the un-doped hybrid (Co_3O_4/rmGO), signifying the importance of nitrogen-doping for making reduced graphene an ORR active material. Additionally, Co_3O_4/N-rmGO was found to demonstrate superior ORR activity compared to Co_3O_4 or N-rmGO alone, indicative of synergistic improvement in the catalytic activity obtained by combining the two materials. The excellent activity of Co_3O_4/N-rmGO is attributed to the strong coupling between the spinel Co_3O_4 nanoparticles on reduced graphene, which was confirmed by C K-edge XANES to show chemical bond formation between Co_3O_4 and N-rmGO. The hybrid material Co_3O_4/N-rmGO demonstrated comparable catalytic activity to the precious metal Pt/C benchmark in both 1.0 M and 6.0 M KOH

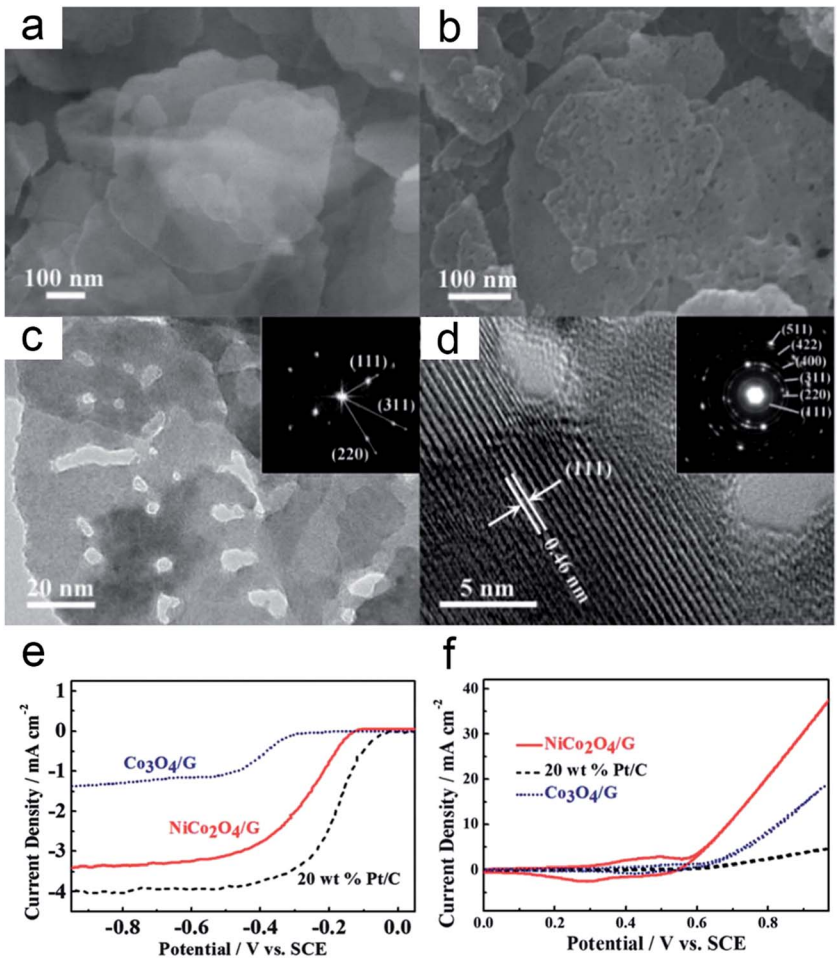

Fig. 8 SEM images of (a) uncalcined $NiCo_2O_4$–G prior to the formation of mesopores, and (b) calcined mesoporous $NiCo_2O_4$–G nanoplatelets. (c) TEM image of $NiCo_2O_4$–G with uniformly distributed mesopores. Inset: the FFT pattern demonstrating spinel $NiCo_2O_4$ structure. (d) HR-TEM image of the (111) crystal plane of spinel $NiCo_2O_4$ nanoplatelets. Inset: the corresponding SAED pattern of $NiCo_2O_4$ nanoplatelets. (e) ORR polarization curves, and (f) OER CV curves of $NiCo_2O_4$–G, Co_3O_4–G and 20 wt% Pt/C obtained at a rotation rate of 900 rpm in an O_2- and N_2-saturated 0.1 M KOH electrolyte, respectively.

electrolytes. In terms of OER, Co_3O_4/N-rmGO was found to perform better than Co_3O_4 and Co_3O_4/rmGO catalysts, resulting in a very small overpotential of 0.31 V obtained at a current density of 10 mA cm^{-2}. The demonstrated results indicate that Co_3O_4/N-rmGO is one of the highest performing bi-functional oxygen catalysts reported to date in the literature.

Catalytic activity enhancement through the modification of carbon support composition was observed in the above section. Similarly, spinel metal oxides composed of more than one cation can be combined with carbon based materials to render bi-functionally effective hybrid catalysts. In the work reported by Chen *et al.* mesoporous $NiCo_2O_4$ nanoplatelets were combined with graphene sheets ($NiCo_2O_4$/G) through a facile one-pot method.[207] Polyvinylpyrrolidone (PVP) was introduced during the synthesis as a capping agent to induce the formation of meso-scale pores in the nanoplatelets to increase the surface area and facilitate transport of reactants during oxygen electrocatalysis (Fig. 8a and b). The TEM image of the nanoplatelet revealed evenly distributed mesopores with the corresponding fast Fourier transform (FFT) pattern demonstrating good crystalline structure (Fig. 8c). Additionally, the high-resolution TEM image revealed lattice fringes which corresponded to the (111) crystal orientation known to be catalytically active for oxygen reactions (Fig. 8d). The activities of $NiCo_2O_4$/G for both ORR and OER were highlighted by a significant improvement over Co_3O_4/G (Fig. 8e and f, respectively). The bi-functional activity improvement was attributed to the formation of highly active reaction sites by the insertion of Ni cations into the octahedral sites of the spinel crystal structure, which increased the electrical conductivity of the catalyst for rapid charge transport during oxygen reactions. Likewise, the composition of spinel oxides is tuned with different cations depending on the specific activity required, and materials cost restrictions.

Similarly, Yan *et al.*[204] reported $FeCo_2O_4$ spinel nanoparticles covalently coupled to hollow structured reduced graphene oxide spheres (FCO/HrGOS), which were prepared step by step *via* an electrostatic assembly method using SiO_2 spheres as the template. The as-designed FCO/HrGOS hybrid demonstrated highly enhanced electrocatalytic activities for both the ORR and OER as compared with FCO and HrGOS tested alone, again indicative of the synergetic effect between $FeCo_2O_4$ and hollow graphene. More importantly, the ORR activity of FCO/HrGOS was comparable to that of the commercial 20 wt% Pt/C catalyst, and its OER activity surpassed that of RuO_2/C. The high ORR and OER activities of FCO/HrGOS hybrid are attributed to the covalent coupling between FCO and HrGOS which provides efficient electron transport paths. Additionally, 3D hollow structured graphene spheres of FCO/HrGOS provide a high surface area and facilitate efficient transport of oxygen and reactants in the electrolyte *via* the increased triple phase (solid–liquid–gas) contact area.

Zhao and co-workers reported a novel method for the synthesis of spinel Mn–Co oxide nanoparticles partially embedded in N-doped CNTs (NCNTs) by oxidative thermal scission.[200] The NCNT encapsulated spinel Mn–Co oxide was grown in the first step, followed by acid leaching to remove the Mn–Co particles that are not intimately in contact with NCNTs. Subsequently, the washed NCNTs still containing the encapsulated catalyst nanoparticles were thermally treated at different temperatures ranging from 300 °C to 600 °C under flowing air to open and rupture the CNTs through oxidation and thermal stress. X-ray photoelectron spectroscopy showed that the surface C and N species did not undergo significant changes even after the high temperature oxidative cutting, while the observation of the O 1s peak at 530.2 eV confirmed the formation of metal oxides. Therefore, the favorable surface properties of NCNTs were not significantly affected by the oxidative cutting conditions while the formation of Mn–Co oxide. The ORR activity of NCNT-500 was significantly improved in comparison to NCNTs, indicating that the Mn–Co oxides formed during oxidative cutting are ORR active. Besides its remarkable ORR activity which is higher than those of IrO_2 and RuO_2, the OER activity of NCNT-500 is very similar to that of RuO_2, making the Mn–Co oxide nanoparticle-embedded NCNTs a highly competitive bifunctional catalyst for reversible oxygen electrodes.

5.3 Perovskite-type metal oxide & carbon material hybrids

A good example of perovskite oxide hybridized with carbon materials is the core–corona structured bifunctional catalyst (CCBC) consisting of the perovskite lanthanum nickelate ($LaNiO_3$) core covered by the porous nitrogen-doped carbon nanotube shell introduced by Chen and co-workers.[209] In this work, the lanthanum nickelate core acts as the OER active component and support material for the growth of NCNTs. The NCNT corona serves as a highly active ORR electrocatalyst and leads to synergistic OER activity. Due to the intrinsically high ORR activity of NCNTs and high OER activity of $LaNiO_3$, as well as the synergistic effect between them, CCBC as a whole demonstrated excellent bifunctional activity and stability compared with Pt/C and $LaNiO_3$ upon half-cell evaluation. Additionally, the hybrid material exhibited excellent charge and discharge rechargeable zinc–air battery performance, comparable to that of precious metal-based catalysts. Later, the same group reported a more optimized hybrid intertwined core–corona structured bifunctional catalyst (IT-CCBC) based on highly tailored nanosized perovskite $LaNiO_3$ nanoparticles to promote more favorable NCNT growth directly on and around the particles.[210] As expected, the SEM (Fig. 9a) and TEM (Fig. 9b) images of IT-CCBC revealed a good coverage of NCNTs over the $LaNiO_3$ nanoparticles, encapsulating them within their porous and intertwined network. The ORR activity of IT-CCBC demonstrated significantly improved onset half-wave potentials, and limiting current density over $LaNiO_3$ particles, and synergistic enhancement of the half-wave potential when compared to NCNT (Fig. 9c), due to improved charge transport and faster diffusion of reactants through the porous carbon network during ORR. Likewise, IT-CCBC demonstrated high OER current density resulting from the synergy of combining $LaNiO_3$ nanoparticles with porous NCNT (Fig. 9d). The unique morphology of IT-CCBC engineered to demonstrate a strong synergy between $LaNiO_3$ and NCNTs resulted in improved rechargeable zinc–air battery performance compared to Pt/C and Ir/C benchmarks in terms of ORR and OER, respectively, as

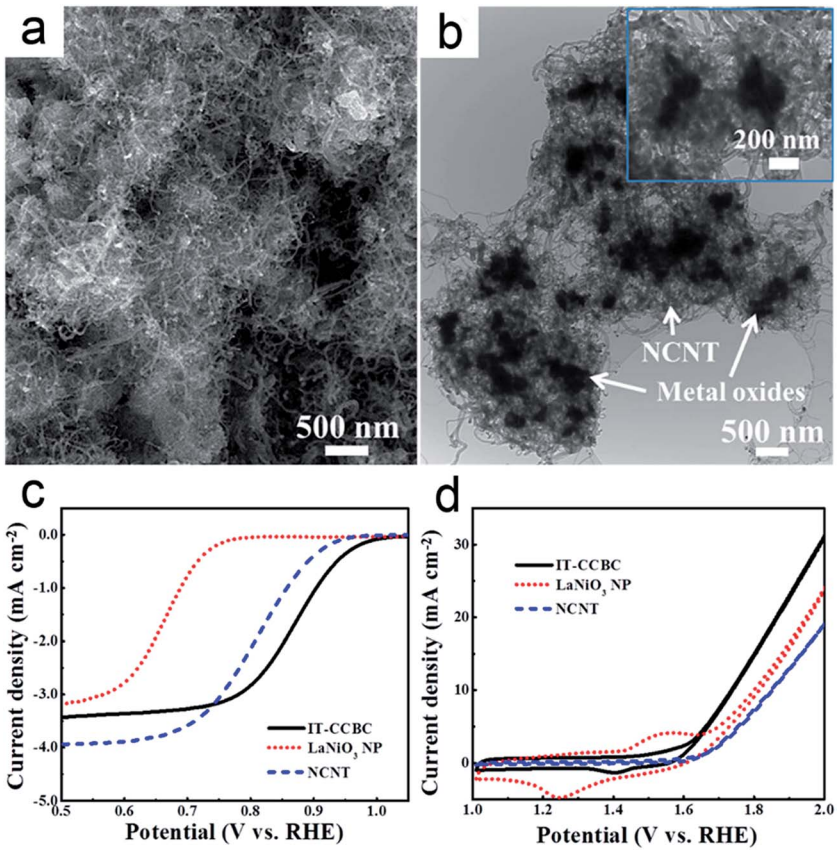

Fig. 9 (a) SEM and (b) TEM images of IT-CCBC. Inset: high magnification image of the composite. (c) ORR, and (d) OER polarization curves of IT-CCBC, $LaNiO_3$ NP, and NCNT obtained at a rotation speed of 900 rpm with 10 mV s^{-1} and 50 mV s^{-1} scan rates, respectively.

well as superior electrochemical stability upon battery cycling. Other than the papers discussed above, there are a few more studies focused on other formulae of perovskites hybridized with carbon materials. For example, La_2O_3 doped on carbonaceous nanospheres,[211] perovskite oxide ($LaCoO_3$ or $La_{0.8}Sr_{0.2}MnO_3$) and carbon thin films,[212] $Ba_{0.5}Sr_{0.5}Co_{0.8}Fe_{0.2}O_{3-\delta}$/carbon composites,[101] $La_{0.5}Sr_{0.5}Co_{0.8}Fe_{0.2}$ nanoparticle (LSCFNP)-based NCNT composites,[213] graphene nanosheet supported $La_{0.5}Ce_{0.5}Fe_{0.5}Mn_{0.5}O_3$,[214] nitrogen-doped carbon nanorod supported $LaTi_{0.65}Fe_{0.35}O_{3-\delta}$ nanoparticles[215] and $La_{0.58}Sr_{0.4}Co_{0.2}Fe_{0.8}O_3$ functionalization with Fe–N/C groups[216] are studied by researchers in regard to their ORR/OER bi-functional activity and application in rechargeable metal air batteries.

5.4 Other types of transition metal compound & carbon material hybrids

As we presented in Section 3.4, other transition metal compounds besides transition metal oxides have also been reported to be bi-functionally active towards ORR and OER, such as transition metals,[217,218] transition metal alloys,[180,219–221] transition metal carbonate hydroxides,[222] nitrides[223] and sulfides.[224,225] This section introduces hybrid bi-functional catalysts based on synergistically combining these materials with carbon materials.

The benefits of improving the interface between transition metal chalcogenides and the carbon support were realized in the work reported by Liu *et al.*, where $NiCo_2S_4$ nanoparticles were grown *in situ* on reduced graphene oxide ($NiCo_2S_4$@N/S-rGO) to obtain an efficient bi-functional catalyst for ORR and OER.[224] The nitrogen and sulfur dopants in $NiCo_2S_4$@N/S-rGO were introduced by using metal salts, thiourea, during one-pot solvothermal graphene oxide reduction in the medium of ethylene glycol. The TEM images of $NiCo_2S_4$@N/S-rGO revealed nanoparticles with an average size of 4–8 nm that are uniformly distributed throughout the graphene sheets without detachment and aggregation (Fig. 10a and b). Additionally, the high resolution TEM image revealed lattice fringes (Fig. 10c) and the crystal orientations observed by the rings of the obtained SAED pattern (Fig. 10d) were consistent with each other. In terms of catalytic activity tested in 0.1 M KOH, $NiCo_2S_4$@N/S-rGO showed inferior ORR activity compared to Pt/C (half-wave potential difference of 47 mV) (Fig. 10e), but significantly improved OER onset potential and current relative to Pt/C (Fig. 10f). For both ORR and OER, the catalytic activity was observed to increase in the order of Ni_3S_4@N/S-rGO, Co_3S_4@N/S-rGO, and $NiCo_2S_4$@N/S-rGO, suggesting better activity of Co–S than Ni–S, and the improvement of bi-functional activity by Ni doping. Additionally, the performance improvement of $NiCo_2S_4$@N/S-rGO is attributed to the coupling interaction between the nanoparticles and the graphene sheets, resulting in

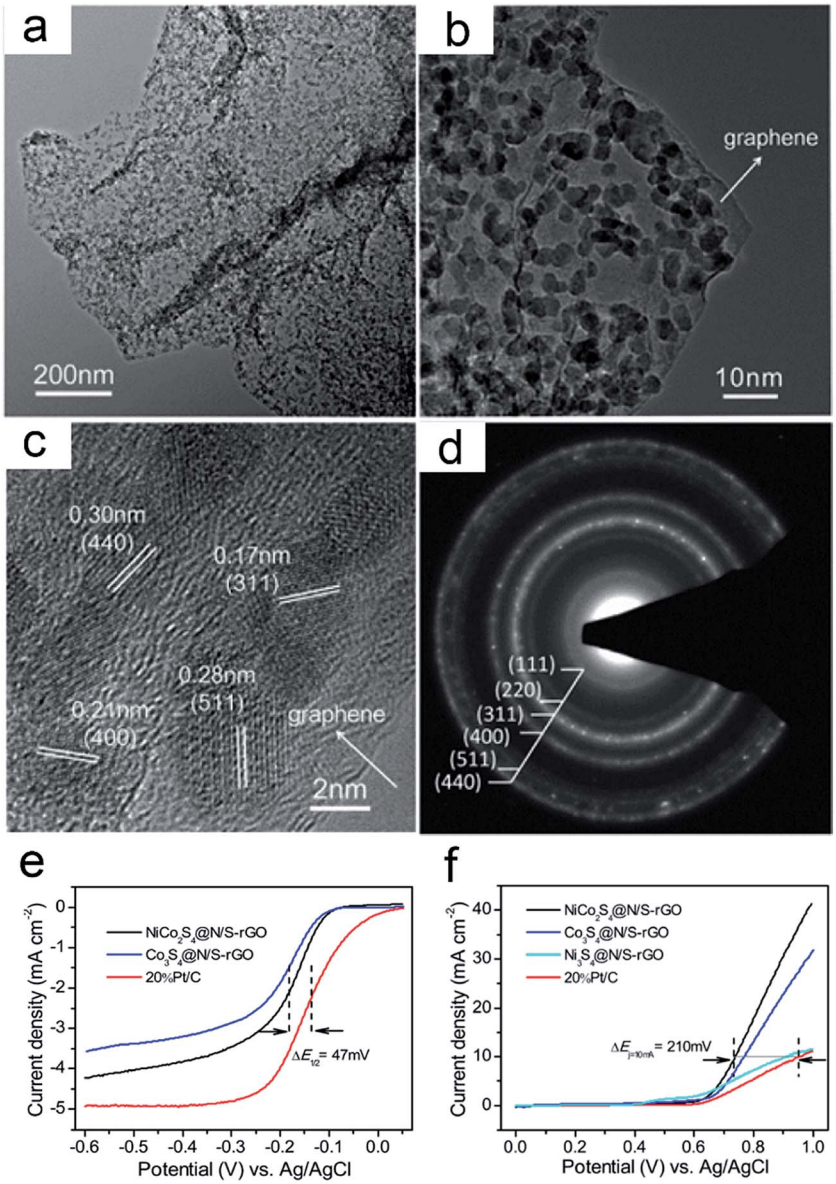

Fig. 10 (a and b) Low-, and (c) high-magnification TEM images of $NiCo_2S_4$@N/S-rGO. (d) Corresponding SAED pattern of $NiCo_2S_4$ nanocrystals grown on graphene sheets. (e) ORR polarization curves of 20% Pt/C, $NiCo_2S_4$@N/S-rGO, and Co_3S_4@N/S-rGO obtained at a rotation rate of 1600 rpm with a sweep rate of 5 mV s^{-1} in an O_2-saturated 0.1 M KOH electrolyte. (f) OER polarization curves of $NiCo_2S_4$@N/S-rGO, Co_3S_4@N/S-rGO, Ni_3S_4@N/S-rGO, and commercial 20% Pt/C obtained at a sweep rate of 10 mV s^{-1} in 0.1 M KOH.

a synergistic effect observed for both ORR and OER when compared to the performance of individual components with the $NiCo_2S_4$@N/S-rGO hybrid. Shen *et al.* developed nanostructured cobalt–iron sulfides covalently entrapped in nitrogen-doped mesoporous graphitic carbon ($Co_{0.5}Fe_{0.5}S$@N-MC) *via* a soft-template mediated approach.[225] This hybrid bi-functional catalyst manifested excellent activity with a half-wave potential of 0.808 V (*vs.* RHE) for ORR, and a current density of 10 mA cm^{-2} at an overpotential as low as 0.41 V for OER. Based on the results of XAS and XPS, the sulfides were found to be covalently bonded to carbon in $Co_{0.5}Fe_{0.5}S$@N-MC. Such covalent bonds acted as anchors for $Co_{0.5}Fe_{0.5}S$ growth, resulting in more homogeneous distribution of $Co_{0.5}Fe_{0.5}S$ and synergetic interaction with a well-defined mesoporous carbon substrate for improved catalytic activity.

A novel cobalt carbonate hydroxide supported on a carbon (CCH/C) catalyst for ORR and OER bi-functional catalysis was reported by Wang and co-workers.[222] Their investigation included the influence of the hydrothermal reaction time on the morphology of CCH/C. With increasing hydrothermal reaction time, CCH in CCH/C transformed from nanorods (CCH/C-2) into a mixture of nanorods and nanosheets (CCH/C-16). The superior performance was obtained with inherently more stable one-dimensional nanorods, making CCH/C-2 a promising bi-functional catalyst with a smaller ORR and OER overpotential gap compared to Pt/C and Ir/C.

Table 1 Summary of ORR and OER activities of recently reported bi-functional oxygen electrocatalysts[a]

Bi-functional catalyst	E_{onset} (V) for ORR	E (V) for ORR (@$j = -3$ mA cm^{-2})	E (V) for OER (@$j = 10$ mA cm^{-2})	$\Delta E_{OER-ORR}$ (V)	Reference	Published year
Non-precious metal-based materials						
Mn oxide	—	0.73	1.77	1.04	19	2010
MnO polyrod	—	0.79	1.81	1.02	23	2015
α-MnO_2-SF	—	0.76	1.72	0.96	25	2014
Meso-Co_3O_4-35	—	0.61	1.64	1.03	50	2013
NCO-A_1	0.93	0.78	1.62	0.84	63	2014
ns$LaNiO_3$	—	0.64	1.66	1.02	81	2013
SL $Ni(OH)_2$	—	0.61 (half-wave potential)	1.53 (@$j = 5$ mA cm^{-2})	0.92	110	2014
SL $Co(OH)_2$	—	0.64 (half-wave potential)	1.57 (@$j = 5$ mA cm^{-2})	0.93	110	2014
CIO-2	0.80	0.75	1.72	0.97	115	2014
Co_3O_4/2.7Co_2MnO_4	0.90	0.68	1.77	1.09	123	2013
Carbon-based materials						
Fe/C/N	0.94	0.81	1.59	0.78	131	2015
N,P-GCNS	1.01	0.86	1.57	0.71	136	2015
CNNT-ACN	0.93	0.71	1.68	0.97	149	2015
NGSH	0.88	0.70	1.63	0.93	159	2014
N-Graphene/CNT	0.88	0.69	1.65	0.96	160	2014
PCN-CFP	0.94	0.72	1.63	0.91	161	2015
Hybrid materials						
Mn_xO_y/NC	—	0.81 (@$j = -1$ mA cm^{-2})	1.68	0.87	167	2014
Co_xO_y/NC	—	0.8 (@$j = -1$ mA cm^{-2})	1.66	0.86	167	2014
Co-CoO/N-rGO	0.88	0.78	1.62	0.84	181	2015
Co_3O_4/N-rmGO	0.88	0.83	1.54	0.71	163	2011
Co_3O_4C-NA	—	0.78 (half-wave potential)	1.52	0.74	183	2014
$CoMn_2O_4$/rGO	0.95	0.89 (@$j = -1$ mA cm^{-2})	1.54	0.65	192	2015
$CoMn_2O_4$/PDDACNTs	0.97	0.83	1.68	0.85	199	2013
C-$CoMn_2$/C		0.75	1.77	1.02	201	2015
$NiCo_2O_4$–G	0.89	0.56	1.69	1.13	207	2013
Co–N/C-800	0.83	0.74	1.6	0.86	218	2014
NCNT/CoONiO–NiCo	0.97	0.83	1.5	0.67	221	2015
CCH-2/C	0.93	0.82	1.74	0.92	222	2014
$NiCo_2S_4$@N/S-rGO	0.85	0.72	1.7	0.98	224	2013
$Co_{0.5}Fe_{0.5}$S@N-MC	0.91	0.81 (half-wave potential)	1.57	0.76	225	2015

[a] All voltages presented in this table are shown *versus* reversible hydrogen electrode (RHE).

6. Current bi-functional catalyst and air electrode development

The above sections discussed recent progress in bi-functional oxygen catalysts based on different material compositions, crystal structures, and geometries. Table 1 shows a summary of ORR and OER activities of some of the recently reported bi-functional catalysts. Traditionally, much of the oxygen catalyst development has been primarily focused on reducing material costs through either reduction of precious metal loading, or replacing precious metal-based catalysts with non-precious metals or metal-free carbon based catalysts. As reported in this review, these new catalyst research efforts are dedicated to further optimizing bi-functional ORR and OER activities to approach those of precious metal benchmarks Pt and Ir based catalysts, respectively. Simultaneously, research efforts have been dedicated to the development of hybrid or composite structured bi-functional catalysts, consisting of both non-precious metal and metal-free carbon materials.[226,227] Hybrid catalysts are interesting because when combined with carbon based materials, the loading of potentially more expensive elements such as Co, Ni, La, and Sr in non-precious metal component can be reduced without severely sacrificing the bi-functional performance of the catalyst. This high catalytic activity of hybrids has been mainly attributed to the synergistic effect, which leads to a superior overall hybrid catalyst activity compared to those of individual components.[163,194,210,213] Synergy in hybrid catalysts has been revealed to be primarily due to highly favorable interaction between the components of a hybrid catalyst. Based on strongly coupled hybrid catalysts, synergistic effects have been observed for both oxygen reduction and evolution reactions. Currently, a part of the bi-functional catalyst development is focused on utilizing the knowledge gained from highly active non-precious metal and metal-free catalysts developed previously, and either combining them or synthesizing them through a one-pot process to obtain favorable interfaces for a synergistic bi-functional catalytic effect.

As an extension to bi-functional catalyst development, incorporating the catalysts into a rechargeable air electrode is currently another field of research receiving tremendous attention. Typically, air electrodes consist of a porous carbon gas diffusion layer, the surface of which is modified (usually by physical deposition) with an active catalyst. For fuel-cells and primary metal–air batteries, this electrode design is sufficient for oxygen gas to diffuse and react at the three phase catalyst/air/electrolyte interface. For rechargeable metal–air batteries, however, the gas diffusion layer which is primarily made of carbon is known to degrade from two different processes simultaneously.[228] The first process, as previously mentioned, is through the electrochemical carbon corrosion which happens during charging of the battery due to large anodic polarization (dependent on the OER overpotential). The second is through mechanical degradation, which occurs due to pressure build up inside the porous carbon during oxygen evolution. Both of these pathways are detrimental to the life of bi-functional air electrodes, significantly reducing the overall lifetime of the battery. To prevent this, advanced bi-functional air electrode designs have been introduced based on using nickel foam filled with nickel powder to form an effective gas diffusion layer.[229,230] This nickel-based electrode completely eliminates the use of carbon, and a $NiCo_2O_4$ bi-functional catalyst layer was simply created by a dip-coating method. Similarly, our recent work reported Co_3O_4 nanowire arrays directly grown on a stainless steel mesh as a carbon and binder-free active electrode for rechargeable zinc–air batteries (Fig. 11a). The stainless steel mesh worked

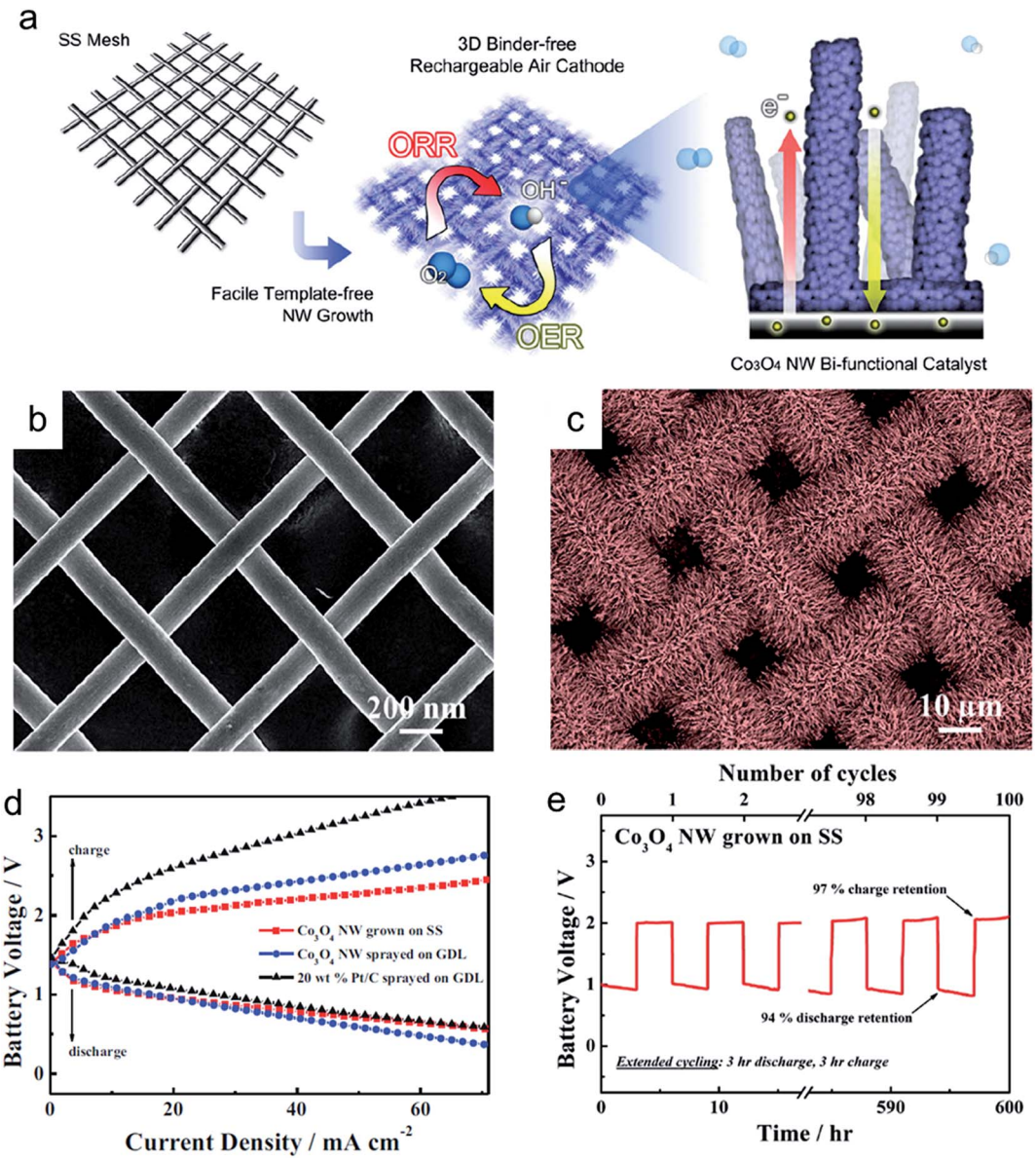

Fig. 11 (a) Schematic illustration of growth of Co_3O_4 nanowires as bi-functionally active oxygen electrocatalyst. SEM images of (b) bare stainless steel (SS) mesh current collector/growth substrate before growth, and (c) densely packed Co_3O_4 nanowires after growth. (d) Single-cell rechargeable zinc–air battery galvanodynamic charge and discharge voltage behaviors, and (e) battery cycling of Co_3O_4 nanowires modified SS bi-functional electrode.

both as a catalyst growth substrate and as a current collector for zinc–air battery (Fig. 11b). After growth, densely packed Co_3O_4 nanowires having an average diameter and length of 300 nm and 15 μm, respectively, were observed (Fig. 11c). The battery demonstrated comparable galvanodynamic discharge behavior to Pt/C (Fig. 11d), as well as a remarkable durability with stable charge and discharge voltages for up to 600 hours of operation (Fig. 11e). Until now, bi-functional oxygen catalyst investigations have been largely carried out in aqueous electrolytes for rechargeable zinc–air batteries. However, bi-functional catalysts in aqueous electrolytes exhibit a strong performance correlation with those in non-aqueous organic electrolytes as well. This has been consistently observed in reports where similar types of bi-functional catalysts mentioned in this review have also employed in non-aqueous electrolyte rechargeable lithium–air batteries. For example, a covalently coupled $MnCo_2O_4$–graphene bi-functional hybrid catalyst tested in a rechargeable lithium–air battery demonstrated 40 stable cycles with a cut-off capacity of 1000 mA h g^{-1} at a current density of 400 mA g^{-1}.[194] Likewise, the bi-functional catalysts discussed in this review can be potentially employed in other types of both aqueous and non-aqueous rechargeable metal–air battery systems.

7. Conclusions and outlook

In conclusion, this review article covers recent research progress in the development of bi-functionally active oxygen electrocatalysts for oxygen reduction and oxygen evolution reactions. The main goal of this research is to replace precious metal-based catalysts with highly active and durable non-precious catalysts for rechargeable metal–air battery applications to harness energy in a cost-effective and scalable manner. In fact, metal–air batteries are considered by far the most promising energy technology for replacing lithium-ion batteries in electric-drive vehicles, not to mention they offer operation safety and environmental benignity. Types of non-precious transition metal-based catalysts introduced in this review include single metal oxides, spinel- and perovskite-type oxides, as well as other transition metal-based compounds such as doped metal oxides, transition metal alloys, hydroxides, nitrides, and sulfides. Most of these catalysts exhibit specific nanostructured morphologies such as nanoparticles, nanorods, and nanowires which lead to increased active surface area and faster diffusion of reactants. Another important class of bi-functional catalysts reviewed in this article is metal-free nanostructured carbon catalysts, which include heteroatom-doped carbon nanotubes and graphene nanosheets. Due to their high electrical conductivity, carbon-based catalysts generally offer superior charge transport properties than oxide-based catalysts during the electrocatalytic oxygen reactions. However, they are more susceptible to degradation due to the corrosion of carbon at high potentials incurred during OER. More recently, hybrid catalysts, which consist of both transition metal- and carbon-based materials, have been introduced. Hybrid catalysts often exhibit synergy between the two components, resulting in catalytic activities that are higher than those obtained individually. This synergistic bi-functional activity is ascribed to the unique coupling between the metal and carbon species, which typically also improves electrochemical durability due to lowered overpotentials. Currently, most bi-functional catalyst research is carried out using alkaline aqueous electrolytes, however, recent literature has shown that their activities are transferrable to non-aqueous electrolytes. This opens the potential application of bi-functional catalysts to a wide range of rechargeable metal–air battery technologies including zinc–air and lithium–air batteries, which are considered highly promising as the next generation low-cost energy conversion and storage systems.

In future bi-functional catalyst developments, researchers will continue to face rather stringent requirements for both performance-to-cost ratio and lifetime of rechargeable metal–air batteries. Currently, the cost of the most widely used lithium-ion batteries has reduced from above $1000 per kW per h to as low as $300 per kW per h after decades of active material development and cell performance testing, analysis, and optimization.[231] Rechargeable metal–air batteries, which boast significantly higher energy density than lithium-ion batteries, are estimated to cost less than $160 per kW per h once commercialized with opportunities in the future to reduce this number through systematic research and development. The key performance attributors which could potentially reduce the cost of rechargeable metal–air batteries are efficiency and durability of bi-functional catalysts. To optimize the performance of bi-functional catalysts, however, the exact mechanism of the electrocatalytic oxygen reactions on the catalyst's surface must be understood through both computational and experimental studies. This would allow effective exploitation of the active sites to maximize the potential of the catalysts, which is why most of the studies reviewed in this article are based on engineering the morphology and composition of bi-functional catalysts.[4,6,12,14,26,232] Engineering the morphology of bi-functional catalysts into nanostructures such as nanotubes, nanorods, and nanowires has proven to be effective for significantly improving the physical properties of a bi-functional catalyst by increasing the degree of active site exposure and the voids between the structures acting as an electrolyte reservoir to rapidly provide reactants during the oxygen electrocatalysis. Fine tuning the catalyst composition, on the other hand, allows modification of the electronic structure of active sites, providing ways for them to optimally interact with oxygen molecules during the reaction. The interaction with oxygen is particularly important for bi-functional catalysts since either too strong or too weak adsorption energy is likely to favor only one of the two reactions. With a plethora of catalyst types, crystal structures, and synthetic routes, the consideration of both morphology and composition for the bi-functional catalyst development is a topic of continuous research.

One area of study on bi-functional catalysts that is currently lagging is the investigation of electrochemical durability, cycle life time and mechanistic pathways that lead to the failure of the catalysts. The fact that bi-functional catalysts allow capability to recharge metal–air batteries ought to lead to charge–discharge cycle tests, but they are absent in most of the articles reviewed in this study. One of the few studies that extensively

investigated the durability of a bi-functional catalyst performed by Chen *et al.* demonstrated both half- and single-cell durability tests as well as post-cycle characterizations to reveal that carbon corrosion during charging was mitigated by hybridizing active carbon nanotubes with highly OER active perovskite oxide catalysts.[209] To the best of our knowledge, no current studies have reported durability investigation through *in situ* physicochemical characterization methods during cycling, which could provide useful information on the changes of the crystal structure, electronic structure and/or morphology of bi-functional catalysts. Upon achieving long lifetime of rechargeable metal–air batteries through successful durability investigations on bi-functional catalysts, this energy system is likely to offer performances that are comparable or even exceed those of existing commercial batteries.

In the early studies of bi-functional catalysts, much effort was focused on metal oxide based materials. Recently, the focus has been shifted to the development of hybrid catalysts which are made of metal oxides coupled with carbon nanostructures. Hybrid catalysts are particularly interesting due to their capability to demonstrate synergistic bi-functional activity and improved durability. However, until now, the synthetic routes of most hybrid bi-functional catalysts required each component to be fabricated separately and then post treated to combine them into one, which significantly increases the time and cost of production.[163,207,209,224,226] Hence, novel one-pot synthesis strategies for hybrid catalysts are a very attractive future research direction since reducing the number of steps can greatly reduce cost during mass production, which would then open doors for widespread commercialization of rechargeable metal–air batteries.

Finally, at present, primary zinc–air batteries are the only type of metal–air battery that found its applications in a niche hearing-aid market. In 2015, the electric drive vehicle market share was only 2.87% over all vehicles sold in the United States despite the tremendous research effort and global initiatives to replace gasoline-powered vehicles and reduce carbon emission.[233] In fact, the US Department of Energy recently launched a $58 million Electric Everywhere Grand Challenge specifically for battery materials and component development to make electric drive vehicles affordable to own and operate as gasoline-powered vehicles by 2022.[234] Upon commercializing rechargeable metal–air batteries through successful bi-functional catalyst development, the electric vehicle market can greatly benefit from this novel energy storage technology since at least 2 to 5 fold higher energy density of metal–air batteries compared to the current state-of-the-art lithium-ion batteries can potentially increase the electric driving range well beyond 270 miles per full charge.[6,235] In addition to electrifying transportation, rechargeable metal–air battery technologies offer enormous benefits in terms of energy security, environmental considerations, and industrial appeal by coupling with intermittent renewable energy sources to generate clean electricity that is carbon emission-free. Renewable energy generation can significantly alleviate the current oil dependence which accounts for 34% of the world's total primary energy source, resulting in 40% of the total CO_2 emission and causing major geopolitical instability.[236] As such, rigorous future bi-functional catalyst research and development must be supported and encouraged to capitalize on this highly promising technology, and continued collaborative efforts from experimentalists, engineers, and environmental scientists are required to overcome the current technical hurdles to realize commercialization of practically viable rechargeable metal–air batteries. Ultimately, this energy technology would allow the current society to move beyond a fossil fuel based economy, encompassing an electric grid and transportation sector that embraces the environment and sustainability.

Author contributions

The manuscript was written through contributions of all authors. All authors have given approval to the final version of the manuscript.

Acknowledgements

Financial support by the Natural Sciences and Engineering Research Council of Canada (NSERC) through grants to Z. C. and the University of Waterloo is gratefully acknowledged.

References

1 Exxon Mobile, *The Outlook for Energy: A View to 2040*, http://corporate.exxonmobil.com/en/energy/energy-outlook, 2016.
2 G. Girishkumar, B. McCloskey, A. Luntz, S. Swanson and W. Wilcke, *J. Phys. Chem. Lett.*, 2010, **1**, 2193–2203.
3 J. S. Lee, S. Tai Kim, R. Cao, N. S. Choi, M. Liu, K. T. Lee and J. Cho, *Adv. Energy Mater.*, 2011, **1**, 34–50.
4 Z.-L. Wang, D. Xu, J.-J. Xu and X.-B. Zhang, *Chem. Soc. Rev.*, 2014, **43**, 7746–7786.
5 V. Neburchilov, H. Wang, J. J. Martin and W. Qu, *J. Power Sources*, 2010, **195**, 1271–1291.
6 Y. Li and H. Dai, *Chem. Soc. Rev.*, 2014, **43**, 5257–5275.
7 L. Roen, C. Paik and T. Jarvi, *Electrochem. Solid-State Lett.*, 2004, **7**, A19–A22.
8 X. Wang, W. Li, Z. Chen, M. Waje and Y. Yan, *J. Power Sources*, 2006, **158**, 154–159.
9 R. Cao, J.-S. Lee, M. Liu and J. Cho, *Adv. Energy Mater.*, 2012, **2**, 816–829.
10 J. S. Spendelow and A. Wieckowski, *Phys. Chem. Chem. Phys.*, 2007, **9**, 2654–2675.
11 P. A. Christensen, A. Hamnett and D. Linares-Moya, *Phys. Chem. Chem. Phys.*, 2011, **13**, 5206–5214.
12 L. Jörissen, *J. Power Sources*, 2006, **155**, 23–32.
13 C. Zinola, A. Arvia, G. Estiu and E. Castro, *J. Phys. Chem.*, 1994, **98**, 7566–7576.
14 F. Cheng and J. Chen, *Chem. Soc. Rev.*, 2012, **41**, 2172–2192.
15 M. Doyle, G. Rajendran, W. Vielstich, H. Gasteiger and A. Lamm, *Fuel Cells Symp. Proc.*, 2003, **3**, 351–395.
16 J. Suntivich, H. A. Gasteiger, N. Yabuuchi, H. Nakanishi, J. B. Goodenough and Y. Shao-Horn, *Nat. Chem.*, 2011, **3**, 546–550.

17 A. Débart, J. Bao, G. Armstrong and P. G. Bruce, *J. Power Sources*, 2007, **174**, 1177–1182.
18 A. Débart, A. J. Paterson, J. Bao and P. G. Bruce, *Angew. Chem.*, 2008, **120**, 4597–4600.
19 Y. Gorlin and T. F. Jaramillo, *J. Am. Chem. Soc.*, 2010, **132**, 13612–13614.
20 Y. Gorlin, B. Lassalle-Kaiser, J. D. Benck, S. Gul, S. M. Webb, V. K. Yachandra, J. Yano and T. F. Jaramillo, *J. Am. Chem. Soc.*, 2013, **135**, 8525–8534.
21 Y. Gorlin, D. Nordlund and T. F. Jaramillo, *ECS Trans.*, 2013, **58**, 735–750.
22 I. Hwang, E. Ahn and Y. Tak, *Int. J. Electrochem. Sci.*, 2014, **9**, 5454–5466.
23 C.-H. Kuo, I. M. Mosa, S. Thanneeru, V. Sharma, L. Zhang, S. Biswas, M. Aindow, S. P. Alpay, J. F. Rusling and S. L. Suib, *Chem. Commun.*, 2015, **51**, 5951–5954.
24 X. Li, A. L. Zhu, W. Qu, H. Wang, R. Hui, L. Zhang and J. Zhang, *Electrochim. Acta*, 2010, **55**, 5891–5898.
25 Y. Meng, W. Song, H. Huang, Z. Ren, S. Y. Chen and S. L. Suib, *J. Am. Chem. Soc.*, 2014, **136**, 11452–11464.
26 V. Nikolova, P. Iliev, K. Petrov, T. Vitanov, E. Zhecheva, R. Stoyanova, I. Valov and D. Stoychev, *J. Power Sources*, 2008, **185**, 727–733.
27 T. Ogasawara, A. Débart, M. Holzapfel, P. Novák and P. G. Bruce, *J. Am. Chem. Soc.*, 2006, **128**, 1390–1393.
28 T. Ohsaka, L. Mao, K. Arihara and T. Sotomura, *Electrochem. Commun.*, 2004, **6**, 273–277.
29 K. Selvakumar, S. M. Senthil Kumar, R. Thangamuthu, G. Kruthika and P. Murugan, *Int. J. Hydrogen Energy*, 2014, **39**, 21024–21036.
30 H. Y. Su, Y. Gorlin, I. C. Man, F. Calle-Vallejo, J. K. Norskov, T. F. Jaramillo and J. Rossmeisl, *Phys. Chem. Chem. Phys.*, 2012, **14**, 14010–14022.
31 X. Wu and K. Scott, *J. Power Sources*, 2012, **206**, 14–19.
32 F. Yin, G. Li and H. Wang, *Catal. Commun.*, 2014, **54**, 17–21.
33 R. Gao, L. Liu, Z. Hu, P. Zhang, X. Cao, B. Wang and X. Liu, *J. Mater. Chem. A*, 2015, **3**, 17598–17605.
34 X. Hu, X. Han, Y. Hu, F. Cheng and J. Chen, *Nanoscale*, 2014, **6**, 3522–3525.
35 Y. Yu, B. Zhang, Z.-L. Xu, Y.-B. He and J.-K. Kim, *Solid State Ionics*, 2014, **262**, 197–201.
36 F. Jiao and H. Frei, *Angew. Chem., Int. Ed.*, 2009, **48**, 1841–1844.
37 F. Jiao and H. Frei, *Chem. Commun.*, 2010, **46**, 2920–2922.
38 M. M. Najafpour, T. Ehrenberg, M. Wiechen and P. Kurz, *Angew. Chem., Int. Ed.*, 2010, **49**, 2233–2237.
39 L. Mao, D. Zhang, T. Sotomura, K. Nakatsu, N. Koshiba and T. Ohsaka, *Electrochim. Acta*, 2003, **48**, 1015–1021.
40 J. Vondrak, B. Klapste, J. Velicka, M. Sedlarikova, J. Reiter, I. Roche, E. Chainet, J. Fauvarque and M. Chatenet, *J. New Mater. Electrochem. Syst.*, 2005, **8**, 209–212.
41 I. Roche, E. Chaînet, M. Chatenet and J. Vondrák, *J. Phys. Chem. C*, 2007, **111**, 1434–1443.
42 M. Hamdani, R. Singh and P. Chartier, *Int. J. Electrochem. Sci.*, 2010, **5**, 556–577.
43 J. Xiao, Q. Kuang, S. Yang, F. Xiao, S. Wang and L. Guo, *Sci. Rep.*, 2013, **3**, 2300.
44 B. S. Yeo and A. T. Bell, *J. Am. Chem. Soc.*, 2011, **133**, 5587–5593.
45 J. G. McAlpin, T. A. Stich, C. A. Ohlin, Y. Surendranath, D. G. Nocera, W. H. Casey and R. D. Britt, *J. Am. Chem. Soc.*, 2011, **133**, 15444–15452.
46 M. De Koninck, S.-C. Poirier and B. Marsan, *J. Electrochem. Soc.*, 2007, **154**, A381–A388.
47 M. De Koninck and B. Marsan, *Electrochim. Acta*, 2008, **53**, 7012–7021.
48 P. W. Menezes, A. Indra, N. R. Sahraie, A. Bergmann, P. Strasser and M. Driess, *ChemSusChem*, 2015, **8**, 164–171.
49 D. U. Lee, J.-Y. Choi, K. Feng, H. W. Park and Z. Chen, *Adv. Energy Mater.*, 2014, **4**, 1301389.
50 Y. J. Sa, K. Kwon, J. Y. Cheon, F. Kleitz and S. H. Joo, *J. Mater. Chem. A*, 2013, **1**, 9992–10001.
51 F. Švegl, B. Orel, I. Grabec-Švegl and V. Kaučič, *Electrochim. Acta*, 2000, **45**, 4359–4371.
52 D. U. Lee, J. Scott, H. W. Park, S. Abureden, J.-Y. Choi and Z. Chen, *Electrochem. Commun.*, 2014, **43**, 109–112.
53 B. Han, D. Qian, M. Risch, H. Chen, M. Chi, Y. S. Meng and Y. Shao-Horn, *J. Phys. Chem. Lett.*, 2015, **6**, 1357–1362.
54 T. Maiyalagan, K. A. Jarvis, S. Therese, P. J. Ferreira and A. Manthiram, *Nat. Commun.*, 2014, **5**, 3949.
55 X. Cao, C. Jin, F. Lu, Z. Yang, M. Shen and R. Yang, *J. Electrochem. Soc.*, 2014, **161**, H296–H300.
56 A. Restovic, E. Ríos, S. Barbato, J. Ortiz and J. L. Gautier, *J. Electroanal. Chem.*, 2002, **522**, 141–151.
57 E. Ríos, H. Reyes, J. Ortiz and J. L. Gautier, *Electrochim. Acta*, 2005, **50**, 2705–2711.
58 Y. Tan, C. Wu, H. Lin, J. Li, B. Chi, J. Pu and L. Jian, *Electrochim. Acta*, 2014, **121**, 183–187.
59 F. Cheng, J. Shen, B. Peng, Y. Pan, Z. Tao and J. Chen, *Nat. Chem.*, 2011, **3**, 79–84.
60 S. Peng, Y. Hu, L. Li, X. Han, F. Cheng, M. Srinivasan, Q. Yan, S. Ramakrishna and J. Chen, *Nano Energy*, 2015, **13**, 718–726.
61 S. Ma, L. Sun, L. Cong, X. Gao, C. Yao, X. Guo, L. Tai, P. Mei, Y. Zeng, H. Xie and R. Wang, *J. Phys. Chem. C*, 2013, **117**, 25890–25897.
62 C. Jin, F. Lu, X. Cao, Z. Yang and R. Yang, *J. Mater. Chem. A*, 2013, **1**, 12170–12177.
63 M. Prabu, K. Ketpang and S. Shanmugam, *Nanoscale*, 2014, **6**, 3173–3181.
64 S. W. T. Price, S. J. Thompson, X. Li, S. F. Gorman, D. Pletcher, A. E. Russell, F. C. Walsh and R. G. A. Wills, *J. Power Sources*, 2014, **259**, 43–49.
65 F. Lu, X. Cao, Y. Wang, C. Jin, M. Shen and R. Yang, *RSC Adv.*, 2014, **4**, 40373–40376.
66 Y. Li, L. Zou, J. Li, K. Guo, X. Dong, X. Li, X. Xue, H. Zhang and H. Yang, *Electrochim. Acta*, 2014, **129**, 14–20.
67 M. De Koninck, S.-C. Poirier and B. Marsan, *J. Electrochem. Soc.*, 2006, **153**, A2103–A2110.
68 M. De Koninck, S.-C. Poirier and B. t. Marsan, *J. Electrochem. Soc.*, 2007, **154**, A381–A388.
69 Y. Liu, L. J. Cao, C. W. Cao, M. Wang, K. L. Leung, S. S. Zeng, T. F. Hung, C. Y. Chung and Z. G. Lu, *Chem. Commun.*, 2014, **50**, 14635–14638.

70 T. F. Hung, S. G. Mohamed, C. C. Shen, Y. Q. Tsai, W. S. Chang and R. S. Liu, *Nanoscale*, 2013, **5**, 12115–12119.
71 J. Ponce, J. L. Rehspringer, G. Poillerat and J. L. Gautier, *Electrochim. Acta*, 2001, **46**, 3373–3380.
72 D. Chen, C. Chen, Z. M. Baiyee, Z. Shao and F. Ciucci, *Chem. Rev.*, 2015, **115**, 9869–9921.
73 J. Sunarso, A. A. Torriero, W. Zhou, P. C. Howlett and M. Forsyth, *J. Phys. Chem. C*, 2012, **116**, 5827–5834.
74 W. G. Hardin, J. T. Mefford, D. A. Slanac, B. B. Patel, X. Wang, S. Dai, X. Zhao, R. S. Ruoff, K. P. Johnston and K. J. Stevenson, *Chem. Mater.*, 2014, **26**, 3368–3376.
75 C. Zhu, A. Nobuta, I. Nakatsugawa and T. Akiyama, *Int. J. Hydrogen Energy*, 2013, **38**, 13238–13248.
76 J. Suntivich, K. J. May, H. A. Gasteiger, J. B. Goodenough and Y. Shao-Horn, *Science*, 2011, **334**, 1383–1385.
77 E. Fabbri, R. Mohamed, P. Levecque, O. Conrad, R. d. Kötz and T. J. Schmidt, *ACS Catal.*, 2014, **4**, 1061–1070.
78 C.-F. Chen, G. King, R. M. Dickerson, P. A. Papin, S. Gupta, W. R. Kellogg and G. Wu, *Nano Energy*, 2015, **13**, 423–432.
79 K. Lopez, G. Park, H.-J. Sun, J.-C. An, S. Eom and J. Shim, *J. Appl. Electrochem.*, 2015, **45**, 313–323.
80 J. Suntivich, E. E. Perry, H. A. Gasteiger and Y. Shao-Horn, *Electrocatalysis*, 2012, **4**, 49–55.
81 W. G. Hardin, D. A. Slanac, X. Wang, S. Dai, K. P. Johnston and K. J. Stevenson, *J. Phys. Chem. Lett.*, 2013, **4**, 1254–1259.
82 K. N. Jung, J. H. Jung, W. B. Im, S. Yoon, K. H. Shin and J. W. Lee, *ACS Appl. Mater. Interfaces*, 2013, **5**, 9902–9907.
83 C. O. Soares, M. D. Carvalho, M. E. Melo Jorge, A. Gomes, R. A. Silva, C. M. Rangel and M. I. da Silva Pereira, *J. Appl. Electrochem.*, 2012, **42**, 325–332.
84 W. Zhou and J. Sunarso, *J. Phys. Chem. Lett.*, 2013, **4**, 2982–2988.
85 X.-Z. Yuan, X. Li, W. Qu, D. G. Ivey and H. Wang, *ECS Trans.*, 2011, **35**, 11–20.
86 N.-L. Wu, W.-R. Liu and S.-J. Su, *Electrochim. Acta*, 2003, **48**, 1567–1571.
87 T. Lippert, M. J. Montenegro, M. Döbeli, A. Weidenkaff, S. Müller, P. R. Willmott and A. Wokaun, *Prog. Solid State Chem.*, 2007, **35**, 221–231.
88 S. Malkhandi, B. Yang, A. K. Manohar, A. Manivannan, G. K. S. Prakash and S. R. Narayanan, *J. Phys. Chem. Lett.*, 2012, **3**, 967–972.
89 H. Arai, S. Müller and O. Haas, *J. Electrochem. Soc.*, 2000, **147**, 3584–3591.
90 O. Haas, F. Holzer, S. Müller, J. M. McBreen, X. Q. Yang, X. Sun and M. Balasubramanian, *Electrochim. Acta*, 2002, **47**, 3211–3217.
91 J. J. Xu, D. Xu, Z. L. Wang, H. G. Wang, L. L. Zhang and X. B. Zhang, *Angew. Chem.*, 2013, **52**, 3887–3890.
92 T. Takeguchi, T. Yamanaka, H. Takahashi, H. Watanabe, T. Kuroki, H. Nakanishi, Y. Orikasa, Y. Uchimoto, H. Takano, N. Ohguri, M. Matsuda, T. Murota, K. Uosaki and W. Ueda, *J. Am. Chem. Soc.*, 2013, **135**, 11125–11130.
93 M. Komo, A. Hagiwara, S. Taminato, M. Hirayama and R. Kanno, *Electrochemistry*, 2012, **80**, 834–838.
94 Y. Zhao, L. Xu, L. Mai, C. Han, Q. An, X. Xu, X. Liu and Q. Zhang, *Proc. Natl. Acad. Sci. U. S. A.*, 2012, **109**, 19569–19574.
95 N. Lin and X. Y. Liu, *Chem. Soc. Rev.*, 2015, **44**, 7881–7915.
96 M. Y. Oh, J. S. Jeon, J. J. Lee, P. Kim and K. S. Nahm, *RSC Adv.*, 2015, **5**, 19190–19198.
97 Y. Zhao, L. Xu, L. Mai, C. Han, Q. An, X. Xu, X. Liu and Q. Zhang, *Proc. Natl. Acad. Sci. U. S. A.*, 2012, **109**, 19569–19574.
98 D. Zhang, Y. Song, Z. Du, L. Wang, Y. Li and J. B. Goodenough, *J. Mater. Chem. A*, 2015, **3**, 9421–9426.
99 J. I. Jung, H. Y. Jeong, M. G. Kim, G. Nam, J. Park and J. Cho, *Adv. Mater.*, 2015, **27**, 266–271.
100 C. Jin, X. Cao, F. Lu, Z. Yang and R. Yang, *Int. J. Hydrogen Energy*, 2013, **38**, 10389–10393.
101 R. Mohamed, E. Fabbri, P. Levecque, R. Kotz, T. J. Schmidt and O. Conrad, *ECS Trans.*, 2014, **58**, 9–18.
102 C. Jin, Z. Yang, X. Cao, F. Lu and R. Yang, *Int. J. Hydrogen Energy*, 2014, **39**, 2526–2530.
103 H. Ohkuma, I. Uechi, N. Imanishi, A. Hirano, Y. Takeda and O. Yamamoto, *J. Power Sources*, 2013, **223**, 319–324.
104 J.-I. Jung, H. Y. Jeong, J.-S. Lee, M. G. Kim and J. Cho, *Angew. Chem.*, 2014, **126**, 4670–4674.
105 M. Risch, K. A. Stoerzinger, S. Maruyama, W. T. Hong, I. Takeuchi and Y. Shao-Horn, *J. Am. Chem. Soc.*, 2014, **136**, 5229–5232.
106 D. N. Leonard, A. Kumar, S. Jesse, M. D. Biegalski, H. M. Christen, E. Mutoro, E. J. Crumlin, Y. Shao-Horn, S. V. Kalinin and A. Y. Borisevich, *Adv. Energy Mater.*, 2013, **3**, 788–797.
107 B. M. Gallant, D. G. Kwabi, R. R. Mitchell, J. Zhou, C. V. Thompson and Y. Shao-Horn, *Energy Environ. Sci.*, 2013, **6**, 2518–2528.
108 J.-H. Lee, R. Black, G. Popov, E. Pomerantseva, F. Nan, G. A. Botton and L. F. Nazar, *Energy Environ. Sci.*, 2012, **5**, 9558–9565.
109 L. D. Rafailović, C. Gammer, C. Rentenberger, T. Trišović, C. Kleber and H. Peter Karnthaler, *Nano Energy*, 2013, **2**, 523–529.
110 L. Wang, C. Lin, D. Huang, F. Zhang, M. Wang and J. Jin, *ACS Appl. Mater. Interfaces*, 2014, **6**, 10172–10180.
111 F. Li, R. Ohnishi, Y. Yamada, J. Kubota, K. Domen, A. Yamada and H. Zhou, *Chem. Commun.*, 2013, **49**, 1175–1177.
112 K. Zhang, L. Zhang, X. Chen, X. He, X. Wang, S. Dong, P. Han, C. Zhang, S. Wang, L. Gu and G. Cui, *J. Phys. Chem. C*, 2013, **117**, 858–865.
113 Z. Zhang, X. Wang, G. Cui, A. Zhang, X. Zhou, H. Xu and L. Gu, *Nanoscale*, 2014, **6**, 3540–3544.
114 Q. Liu and J. Zhang, *CrystEngComm*, 2013, **15**, 5087–5092.
115 A. Indra, P. W. Menezes, N. R. Sahraie, A. Bergmann, C. Das, M. Tallarida, D. Schmeisser, P. Strasser and M. Driess, *J. Am. Chem. Soc.*, 2014, **136**, 17530–17536.
116 P. H. Benhangi, A. Alfantazi and E. Gyenge, *Electrochim. Acta*, 2014, **123**, 42–50.
117 M. De Koninck, P. Manseau and B. Marsan, *J. Electroanal. Chem.*, 2007, **611**, 67–79.
118 G. Du, X. Liu, Y. Zong, T. S. Hor, A. Yu and Z. Liu, *Nanoscale*, 2013, **5**, 4657–4661.
119 D. N. Leonard, A. Kumar, S. Jesse, M. D. Biegalski, H. M. Christen, E. Mutoro, E. J. Crumlin, Y. Shao-Horn,

S. V. Kalinin and A. Y. Borisevich, *Adv. Energy Mater.*, 2013, **3**, 788–797.
120 V. Rashkova, S. Kitova, I. Konstantinov and T. Vitanov, *Electrochim. Acta*, 2002, **47**, 1555–1560.
121 V. Rashkova, S. Kitova and T. Vitanov, *Electrochim. Acta*, 2007, **52**, 3794–3803.
122 M. Risch, K. A. Stoerzinger, S. Maruyama, W. T. Hong, I. Takeuchi and Y. Shao-Horn, *J. Am. Chem. Soc.*, 2014, **136**, 5229–5232.
123 D. Wang, X. Chen, D. G. Evans and W. Yang, *Nanoscale*, 2013, **5**, 5312–5315.
124 W. Yang, J. Salim, S. Li, C. Sun, L. Chen, J. B. Goodenough and Y. Kim, *J. Mater. Chem.*, 2012, **22**, 18902–18907.
125 M. Yuasa, M. Nishida, T. Kida, N. Yamazoe and K. Shimanoe, *J. Electrochem. Soc.*, 2011, **158**, A605–A610.
126 J. P. Paraknowitsch and A. Thomas, *Energy Environ. Sci.*, 2013, **6**, 2839–2855.
127 J. D. Baran, H. Gronbeck and A. Hellman, *J. Am. Chem. Soc.*, 2014, **136**, 1320–1326.
128 F. Calle-Vallejo, J. I. Martínez, J. M. García-Lastra, E. Abad and M. T. M. Koper, *Surf. Sci.*, 2013, **607**, 47–53.
129 J. L. Shui, N. K. Karan, M. Balasubramanian, S. Y. Li and D. J. Liu, *J. Am. Chem. Soc.*, 2012, **134**, 16654–16661.
130 D. Sun, Y. Shen, W. Zhang, L. Yu, Z. Yi, W. Yin, D. Wang, Y. Huang, J. Wang, D. Wang and J. B. Goodenough, *J. Am. Chem. Soc.*, 2014, **136**, 8941–8946.
131 Y. Zhao, K. Kamiya, K. Hashimoto and S. Nakanishi, *J. Phys. Chem. C*, 2015, **119**, 2583–2588.
132 E. Yoo and H. Zhou, *J. Power Sources*, 2013, **244**, 429–434.
133 T. Belytschko, S. P. Xiao, G. C. Schatz and R. S. Ruoff, *Phys. Rev. B: Condens. Matter Mater. Phys.*, 2002, **65**, 235430.
134 M. J. Allen, V. C. Tung and R. B. Kaner, *Chem. Rev.*, 2010, **110**, 132–145.
135 M. Li, L. Zhang, Q. Xu, J. Niu and Z. Xia, *J. Catal.*, 2014, **314**, 66–72.
136 R. Li, Z. Wei and X. Gou, *ACS Catal.*, 2015, **5**, 4133–4142.
137 Z. Lin, G. H. Waller, Y. Liu, M. Liu and C.-p. Wong, *Nano Energy*, 2013, **2**, 241–248.
138 Z. Lin, G. H. Waller, Y. Liu, M. Liu and C.-p. Wong, *Carbon*, 2013, **53**, 130–136.
139 B. Sun, B. Wang, D. Su, L. Xiao, H. Ahn and G. Wang, *Carbon*, 2012, **50**, 727–733.
140 E. Yoo and H. Zhou, *ACS Nano*, 2011, **5**, 3020–3026.
141 D. Y. Kim, M. Kim, D. W. Kim, J. Suk, O. O. Park and Y. Kang, *Carbon*, 2015, **93**, 625–635.
142 Y. Li, J. Wang, X. Li, D. Geng, M. N. Banis, R. Li and X. Sun, *Electrochem. Commun.*, 2012, **18**, 12–15.
143 Y. Li, J. Wang, X. Li, D. Geng, M. N. Banis, Y. Tang, D. Wang, R. Li, T.-K. Sham and X. Sun, *J. Mater. Chem.*, 2012, **22**, 20170–20174.
144 Y. Li, H. Yadegari, X. Li, M. N. Banis, R. Li and X. Sun, *Chem. Commun.*, 2013, **49**, 11731–11733.
145 E. Yoo and H. Zhou, *RSC Adv.*, 2014, **4**, 13119–13122.
146 Y. Cheng, Y. Tian, X. Fan, J. Liu and C. Yan, *Electrochim. Acta*, 2014, **143**, 291–296.
147 Y. Cheng, J. Zhang and S. P. Jiang, *Chem. Commun.*, 2015, **51**, 13764–13767.
148 G.-L. Tian, Q. Zhang, B. Zhang, Y.-G. Jin, J.-Q. Huang, D. S. Su and F. Wei, *Adv. Funct. Mater.*, 2014, **24**, 5956–5961.
149 R. M. Yadav, J. Wu, R. Kochandra, L. Ma, C. S. Tiwary, L. Ge, G. Ye, R. Vajtai, J. Lou and P. M. Ajayan, *ACS Appl. Mater. Interfaces*, 2015, **7**, 11991–12000.
150 R. E. Fuentes, H. R. Colón-Mercado and E. B. Fox, *J. Power Sources*, 2014, **255**, 219–222.
151 Y. Li, Z. Huang, K. Huang, D. Carnahan and Y. Xing, *Energy Environ. Sci.*, 2013, **6**, 3339–3345.
152 W. Zhang, F. Liang, C. Li, L.-G. Qiu, Y.-P. Yuan, F.-M. Peng, X. Jiang, A.-J. Xie, Y.-H. Shen and J.-F. Zhu, *J. Hazard. Mater.*, 2011, **186**, 984–990.
153 Y. Li, X. Li, D. Geng, Y. Tang, R. Li, J.-P. Dodelet, M. Lefèvre and X. Sun, *Carbon*, 2013, **64**, 170–177.
154 K. Sakaushi, T. P. Fellinger and M. Antonietti, *ChemSusChem*, 2015, **8**, 1156–1160.
155 Z. Guo, D. Zhou, X. Dong, Z. Qiu, Y. Wang and Y. Xia, *Adv. Mater.*, 2013, **25**, 5668–5672.
156 M. Wang, Y. Lai, J. Fang, J. Li, F. Qin, K. Zhang and H. Lu, *Int. J. Hydrogen Energy*, 2015, **40**, 16230–16237.
157 J. Zhang, Z. Zhao, Z. Xia and L. Dai, *Nat. Nanotechnol.*, 2015, **10**, 444–452.
158 H. W. Park, D. U. Lee, Y. Liu, J. Wu, L. F. Nazar and Z. Chen, *J. Electrochem.Soc.*, 2013, **160**, A2244–A2250.
159 G. L. Tian, M. Q. Zhao, D. Yu, X. Y. Kong, J. Q. Huang, Q. Zhang and F. Wei, *Small*, 2014, **10**, 2251–2259.
160 Z. Wen, S. Ci, Y. Hou and J. Chen, *Angew. Chem., Int. Ed.*, 2014, **53**, 6496–6500.
161 T. Y. Ma, J. Ran, S. Dai, M. Jaroniec and S. Z. Qiao, *Angew. Chem., Int. Ed.*, 2015, **54**, 4646–4650.
162 Y. Liang, H. Wang, J. Zhou, Y. Li, J. Wang, T. Regier and H. Dai, *J. Am. Chem. Soc.*, 2012, **134**, 3517–3523.
163 Y. Liang, Y. Li, H. Wang, J. Zhou, J. Wang, T. Regier and H. Dai, *Nat. Mater.*, 2011, **10**, 780–786.
164 Z. Chen, A. Yu, R. Ahmed, H. Wang, H. Li and Z. Chen, *Electrochim. Acta*, 2012, **69**, 295–300.
165 D. Ye, T. Wu, H. Cao, Y. Wang, B. Liu, S. Zhang and J. Kong, *RSC Adv.*, 2015, **5**, 26710–26715.
166 G. Q. Zhang, J. P. Zheng, R. Liang, C. Zhang, B. Wang, M. Au, M. Hendrickson and E. J. Plichta, *J. Electrochem. Soc.*, 2011, **158**, A822–A827.
167 J. Masa, W. Xia, I. Sinev, A. Zhao, Z. Sun, S. Grutzke, P. Weide, M. Muhler and W. Schuhmann, *Angew. Chem., Int. Ed.*, 2014, **53**, 8508–8512.
168 Y. Cao, Z. Wei, J. He, J. Zang, Q. Zhang, M. Zheng and Q. Dong, *Energy Environ. Sci.*, 2012, **5**, 9765–9768.
169 H. Cheng and K. Scott, *J. Power Sources*, 2010, **195**, 1370–1374.
170 A. Sumboja, X. Ge, F. W. T. Goh, B. Li, D. Geng, T. S. A. Hor, Y. Zong and Z. Liu, *ChemPlusChem*, 2015, **80**, 1341–1346.
171 H.-Q. Wang, J. Chen, S.-J. Hu, X.-H. Zhang, X.-P. Fan, J. Du, Y.-G. Huang and Q.-Y. Li, *RSC Adv.*, 2015, **5**, 72495–72499.
172 Y. Yang, M. Shi, Y. S. Li and Z. W. Fu, *J. Electrochem. Soc.*, 2012, **159**, A1917–A1921.
173 Y. Yu, B. Zhang, Y.-B. He, Z.-D. Huang, S.-W. Oh and J.-K. Kim, *J. Mater. Chem. A*, 2013, **1**, 1163–1170.

174 N. I. Andersen, A. Serov and P. Atanassov, *Appl. Catal., B*, 2015, **163**, 623–627.
175 S. Jee, W. Choi, C. H. Ahn, G. Yang, H. K. Cho, J.-H. Lee and C. Yu, *J. Mater. Chem. A*, 2015, 13767–13775.
176 W. Chen, Z. Zhang, W. Bao, Y. Lai, J. Li, Y. Gan and J. Wang, *Electrochim. Acta*, 2014, **134**, 293–301.
177 W. Chaikittisilp, N. L. Torad, C. Li, M. Imura, N. Suzuki, S. Ishihara, K. Ariga and Y. Yamauchi, *Chem.–Eur. J.*, 2014, **20**, 4217–4221.
178 S. Mao, Z. Wen, T. Huang, Y. Hou and J. Chen, *Energy Environ. Sci.*, 2014, **7**, 609–616.
179 B.-W. Huang, L. Li, Y.-J. He, X.-Z. Liao, Y.-S. He, W. Zhang and Z.-F. Ma, *Electrochim. Acta*, 2014, **137**, 183–189.
180 Y. Li, M. Gong, Y. Liang, J. Feng, J. E. Kim, H. Wang, G. Hong, B. Zhang and H. Dai, *Nat. Commun.*, 2013, **4**, 1805.
181 X. Liu, W. Liu, M. Ko, M. Park, M. G. Kim, P. Oh, S. Chae, S. Park, A. Casimir, G. Wu and J. Cho, *Adv. Funct. Mater.*, 2015, **25**, 5799–5808.
182 J. Yin, J. M. Carlin, J. Kim, Z. Li, J. H. Park, B. Patel, S. Chakrapani, S. Lee and Y. L. Joo, *Adv. Energy Mater.*, 2015, **5**, 1401412.
183 T. Y. Ma, S. Dai, M. Jaroniec and S. Z. Qiao, *J. Am. Chem. Soc.*, 2014, **136**, 13925–13931.
184 W. H. Ryu, T. H. Yoon, S. H. Song, S. Jeon, Y. J. Park and I. D. Kim, *Nano Lett.*, 2013, **13**, 4190–4197.
185 C. Sun, F. Li, C. Ma, Y. Wang, Y. Ren, W. Yang, Z. Ma, J. Li, Y. Chen, Y. Kim and L. Chen, *J. Mater. Chem. A*, 2014, **2**, 7188–7196.
186 C. Zhang, M. Antonietti and T.-P. Fellinger, *Adv. Funct. Mater.*, 2014, **24**, 7655–7665.
187 T. An, X. Ge, T. S. A. Hor, F. W. T. Goh, D. Geng, G. Du, Y. Zhan, Z. Liu and Y. Zong, *RSC Adv.*, 2015, **5**, 75773–75780.
188 B. Li, X. Ge, F. W. Goh, T. S. Hor, D. Geng, G. Du, Z. Liu, J. Zhang, X. Liu and Y. Zong, *Nanoscale*, 2015, **7**, 1830–1838.
189 Q.-c. Liu, J.-j. Xu, Z.-w. Chang and X.-b. Zhang, *J. Mater. Chem. A*, 2014, **2**, 6081–6085.
190 M. J. Song, I. T. Kim, Y. B. Kim and M. W. Shin, *Electrochim. Acta*, 2015, **182**, 289–296.
191 J. Zhang, P. Li, Z. Wang, J. Qiao, D. Rooney, W. Sun and K. Sun, *J. Mater. Chem. A*, 2015, **3**, 1504–1510.
192 J. Du, C. Chen, F. Cheng and J. Chen, *Inorg. Chem.*, 2015, **54**, 5467–5474.
193 X. Ge, Y. Liu, F. W. Goh, T. S. Hor, Y. Zong, P. Xiao, Z. Zhang, S. H. Lim, B. Li, X. Wang and Z. Liu, *ACS Appl. Mater. Interfaces*, 2014, **6**, 12684–12691.
194 Y. Liang, H. Wang, J. Zhou, Y. Li, J. Wang, T. Regier and H. Dai, *J. Am. Chem. Soc.*, 2012, **134**, 3517–3523.
195 M. Prabu, P. Ramakrishnan and S. Shanmugam, *Electrochem. Commun.*, 2014, **41**, 59–63.
196 H. Wang, Y. Yang, Y. Liang, G. Zheng, Y. Li, Y. Cui and H. Dai, *Energy Environ. Sci.*, 2012, **5**, 7931–7935.
197 L. Wang, X. Zhao, Y. Lu, M. Xu, D. Zhang, R. S. Ruoff, K. J. Stevenson and J. B. Goodenough, *J. Electrochem. Soc.*, 2011, **158**, A1379–A1382.
198 C. Xu, M. Lu, Y. Zhan and J. Y. Lee, *RSC Adv.*, 2014, **4**, 25089–25092.
199 X. Zhai, W. Yang, M. Li, G. Lv, J. Liu and X. Zhang, *Carbon*, 2013, **65**, 277–286.
200 A. Zhao, J. Masa, W. Xia, A. Maljusch, M. G. Willinger, G. Clavel, K. Xie, R. Schlogl, W. Schuhmann and M. Muhler, *J. Am. Chem. Soc.*, 2014, **136**, 7551–7554.
201 C. Li, X. Han, F. Cheng, Y. Hu, C. Chen and J. Chen, *Nat. Commun.*, 2015, **6**, 7345.
202 W. Bian, Z. Yang, P. Strasser and R. Yang, *J. Power Sources*, 2014, **250**, 196–203.
203 S. Liu, W. Bian, Z. Yang, J. Tian, C. Jin, M. Shen, Z. Zhou and R. Yang, *J. Mater. Chem. A*, 2014, **2**, 18012–18017.
204 W. Yan, Z. Yang, W. Bian and R. Yang, *Carbon*, 2015, **92**, 74–83.
205 Y. Zhan, C. Xu, M. Lu, Z. Liu and J. Y. Lee, *J. Mater. Chem. A*, 2014, **2**, 16217–16223.
206 W. Yan, X. Cao, J. Tian, C. Jin, K. Ke and R. Yang, *Carbon*, 2015, **99**, 195–202.
207 D. U. Lee, B. J. Kim and Z. Chen, *J. Mater. Chem. A*, 2013, **1**, 4754–4762.
208 H. Zhang, H. Qiao, H. Wang, N. Zhou, J. Chen, Y. Tang, J. Li and C. Huang, *Nanoscale*, 2014, **6**, 10235–10242.
209 Z. Chen, A. Yu, D. Higgins, H. Li, H. Wang and Z. Chen, *Nano Lett.*, 2012, **12**, 1946–1952.
210 D. U. Lee, H. W. Park, M. G. Park, V. Ismayilov and Z. Chen, *ACS Appl. Mater. Interfaces*, 2015, **7**, 902–910.
211 X. Zhang, Q. Xiao, Y. Zhang, X. Jiang, Z. Yang, Y. Xue, Y.-M. Yan and K. Sun, *J. Phys. Chem. C*, 2014, **118**, 20229–20237.
212 T. Poux, F. S. Napolskiy, T. Dintzer, G. Kéranguéven, S. Y. Istomin, G. A. Tsirlina, E. V. Antipov and E. R. Savinova, *Catal. Today*, 2012, **189**, 83–92.
213 H. W. Park, D. U. Lee, M. G. Park, R. Ahmed, M. H. Seo, L. F. Nazar and Z. Chen, *ChemSusChem*, 2015, **8**, 1058–1065.
214 L. Wang, M. Ara, K. Wadumesthrige, S. Salley and K. Y. S. Ng, *J. Power Sources*, 2013, **234**, 8–15.
215 M. Prabu, P. Ramakrishnan, P. Ganesan, A. Manthiram and S. Shanmugam, *Nano Energy*, 2015, **15**, 92–103.
216 R. A. Rincon, J. Masa, S. Mehrpour, F. Tietz and W. Schuhmann, *Chem. Commun.*, 2014, **50**, 14760–14762.
217 Z. Zhang, L. Su, M. Yang, M. Hu, J. Bao, J. Wei and Z. Zhou, *Chem. Commun.*, 2014, **50**, 776–778.
218 Y. Su, Y. Zhu, H. Jiang, J. Shen, X. Yang, W. Zou, J. Chen and C. Li, *Nanoscale*, 2014, **6**, 15080–15089.
219 B.-W. Huang, X.-Z. Liao, H. Wang, C.-N. Wang, Y.-S. He and Z.-F. Ma, *J. Electrochem. Soc.*, 2013, **160**, A1112–A1117.
220 Z. Chen, J.-Y. Choi, H. Wang, H. Li and Z. Chen, *J. Power Sources*, 2011, **196**, 3673–3677.
221 X. Liu, M. Park, M. G. Kim, S. Gupta, G. Wu and J. Cho, *Angew. Chem.*, 2015, **54**, 9654–9658.
222 Y. Wang, W. Ding, S. Chen, Y. Nie, K. Xiong and Z. Wei, *Chem. Commun.*, 2014, **50**, 15529–15532.
223 S. Dong, X. Chen, K. Zhang, L. Gu, L. Zhang, X. Zhou, L. Li, Z. Liu, P. Han, H. Xu, J. Yao, C. Zhang, X. Zhang, C. Shang, G. Cui and L. Chen, *Chem. Commun.*, 2011, **47**, 11291–11293.
224 Q. Liu, J. Jin and J. Zhang, *ACS Appl. Mater. Interfaces*, 2013, **5**, 5002–5008.

225 M. Shen, C. Ruan, Y. Chen, C. Jiang, K. Ai and L. Lu, *ACS Appl. Mater. Interfaces*, 2015, **7**, 1207–1218.
226 Y. Liang, Y. Li, H. Wang and H. Dai, *J. Am. Chem. Soc.*, 2013, **135**, 2013–2036.
227 H. Wang and H. Dai, *Chem. Soc. Rev.*, 2013, **42**, 3088–3113.
228 G. Toussaint, P. Stevens, L. Akrour, R. Rouget and F. Fourgeot, *ECS Trans.*, 2010, **28**, 25–34.
229 X. Li, D. Pletcher, A. E. Russell, F. C. Walsh, R. G. Wills, S. F. Gorman, S. W. Price and S. J. Thompson, *Electrochem. Commun.*, 2013, **34**, 228–230.
230 S. W. Price, S. J. Thompson, X. Li, S. F. Gorman, D. Pletcher, A. E. Russell, F. C. Walsh and R. G. Wills, *J. Power Sources*, 2014, **259**, 43–49.
231 B. Nykvist and M. Nilsson, *Nat. Clim. Change*, 2015, **5**, 329–332.
232 M. A. Rahman, X. Wang and C. Wen, *J. Electrochem. Soc.*, 2013, **160**, A1759–A1771.
233 Electric Drive Transportation Association (EDTA), Total Electric Drive Market Share, http://electricdrive.org/index.php?ht=d/sp/i/20952/pid/20952, 2016.
234 Department of Energy, http://energy.gov/articles/energy-department-announces-58-million-advance-fuel-efficient-vehicle-technologies, 2016.
235 G. Girishkumar, B. McCloskey, A. C. Luntz, S. Swanson and W. Wilcke, *J. Phys. Chem. Lett.*, 2010, **1**, 2193–2203.
236 B. Richter, D. Goldston, G. Crabtree, L. Glicksman, D. Goldstein, D. Greene, D. Kammen, M. Levine, M. Lubell, M. Savitz, D. Sperling, F. Schlachter, J. Scofield and J. Dawson, *Rev. Mod. Phys.*, 2008, **80**, S1–S109.